

A Systematic Study of Electron-Phonon Coupling to Oxygen Modes Across the Cuprates

S. Johnston¹, F. Vernay², B. Moritz^{3,4}, Z.-X. Shen^{3,5,6}, N. Nagaosa^{7,8}, J. Zaanen⁹, and T. P. Devereaux^{3,5}

¹*IFW Dresden, P.O. Box 27 01 16, D-01171 Dresden, Germany*

²*LAMPS, Université de Perpignan Via Domitia, 66860 Perpignan Cedex, France*

³*Stanford Institute for Materials and Energy Science,*

SLAC National Accelerator Laboratory and Stanford University, Stanford, CA 94305, USA

⁴*Department of Physics and Astrophysics, University of North Dakota, Grand Forks, ND 58202, USA*

⁵*Geballe Laboratory for Advanced Materials, Stanford University, Stanford, CA 94305, USA*

⁶*Department of Physics and Applied Physics, Stanford University, CA 94305, USA*

⁷*Department of Applied Physics, University of Tokyo, Bunkyo-ku, Tokyo 113-8656, Japan*

⁸*Cross-Correlated Materials Research Group (CMRG) and Correlated*

Electron Research Group (CERG), RIKEN-ASI, Wako 351-0198, Japan and

⁹*Leiden Institute of Physics, Leiden University, 2333CA Leiden, The Netherlands*

(Dated: October 25, 2018)

The large variations of T_c across the cuprate families is one of the major unsolved puzzles in condensed matter physics, and is poorly understood. Although there appears to be a great deal of universality in the cuprates, several orders of magnitude changes in T_c can be achieved through changes in the chemical composition and structure of the unit cell. In this paper we formulate a systematic examination of the variations in electron-phonon coupling to oxygen phonons in the cuprates, incorporating a number of effects arising from several aspects of chemical composition and doping across cuprate families. It is argued that the electron-phonon coupling is a very sensitive probe of the material-dependent variations of chemical structure, affecting the orbital character of the band crossing the Fermi level, the strength of local electric fields arising from structural-induced symmetry breaking, doping dependent changes in the underlying band structure, and ionicity of the crystal governing the ability of the material to screen c -axis perturbations. Using electrostatic Ewald calculations and known experimental structural data, we establish a connection between the material's maximal T_c at optimal doping and the strength of coupling to c -axis modes. We demonstrate that materials with the largest coupling to the out-of-phase bond-buckling (" B_{1g} ") oxygen phonon branch also have the largest T_c 's. In light of this observation we present model T_c calculations using a two-well model where phonons work in conjunction with a dominant pairing interaction, presumably due to spin fluctuations, indicating how phonons can generate sizeable enhancements to T_c despite the relatively small coupling strengths. Combined, these results can provide a natural framework for understanding the doping and material dependence of T_c across the cuprates.

PACS numbers: 74.72.Gh, 71.38.-k, 74.78.-w

I. INTRODUCTION

Due to the extensive studies on the physical properties of the cuprates, many constraints on the pairing mechanism of their high-temperature superconductivity (HTSC) have been accumulated. There is no doubt that the strong Coulomb interaction and the resultant strong electron correlations play crucial roles. This effect is believed to be described by single-band Hubbard or t - J models in 2D, and the magnetic mechanism for superconductivity has been proposed with the focus on the short range antiferromagnetism or spin singlet formation.¹ These models have achieved great success in explaining many of the physical properties, such as the pseudogap, generalized magnetic susceptibility observed by neutron scattering, and the single particle Green's function found in angle-resolved photoemission spectra (ARPES). However, these models are not successful in explaining the variation of in superconducting transition temperature T_c from material to material and other ma-

terial dependent properties. For example, the famous T-linear resistivity within the plane is universally observed among various cuprates, while T_c 's differ by two orders of magnitude.^{2,3} It is surprising that the resistivity, which is one of the most representative physical observables of the electronic states in solids, is irrelevant to T_c . The 2D Hubbard and t - J models contain only a few parameters, such as hopping parameters t , t' , t'' and interactions U and J . One possibility is that the range of the hopping and magnitude of t' and t'' are key factors determining T_c , which is determined by the structure and chemical composition perpendicular to the CuO_2 plane.⁴ However, studies on the t - J model have found that finite t' suppresses superconducting correlations.⁵ Recent investigations of the single-band Hubbard model using cluster dynamical mean field theory calculations⁶ do not show increased tendencies towards pairing for larger t' but variational studies do,⁷ although the latter may be less controlled.

From a structural point of view, the only known empirical rule of T_c is that it increases at optimal doping

as the number of CuO_2 layers n is increased for $n < 3$. Anderson noticed this n -dependence at an early stage, and proposed the interlayer mechanism of superconductivity.⁸ The idea is that the single-particle interlayer hopping is suppressed by strong correlations within the layer, while the two-particle hopping is not. The onset of the latter below T_c leads to the condensation energy of superconductivity. Experimentally it is found that the c -axis electron hopping is actually suppressed and there is no coherent band formation perpendicular to the plane.³ There is no plasmon observed in the normal state, and below T_c the Josephson plasmon appears in the low energy region (~ 10 meV).⁹ The idea of an interlayer mechanism has also been criticized in light of the c -axis oscillator strength, and has subsequently been abandoned.¹⁰

Increasing evidence for the importance of out-of-plane effects continues to accrue, which points to limitations of intrinsic planar models for the cuprates. For example, the correlation of out-of-phase oxygen dopant ions in $\text{Bi}_2\text{Sr}_2\text{CaCu}_2\text{O}_{8+\delta}$ (Bi-2212) with features in the tunneling density of states¹¹ has been interpreted in terms of a local increase of the superconducting pair potential.¹² In addition, the rapid suppression of T_c with out-of-plane cation dopants compared to in-plane dopants is surprising given that the former do not appreciably affect in-plane resistivities.^{13,14} T_c has also been empirically correlated with the Madelung energy difference between apical and planar oxygen atoms.¹⁵ This has been recently supported by studies on $\text{Ba}_2\text{Ca}_3\text{Cu}_4\text{O}_8\text{F}_2$, a compound which has vastly different transition temperatures by exchanging F with O at the apical site.¹⁶ ARPES studies have inferred a pairing gap which is a factor of 2 larger on the bonding band in comparison to the antibonding band,¹⁷ a trend consistent with other cuprates.¹⁸ Since the Fermi surface of the bonding band lies far away from either the antiferromagnetic reciprocal lattice zone boundary, or the van Hove points, linking the pairing mechanism with a purely electronic mechanism is not straightforward.

As discussed in Refs. 4 and 15, the Madelung energy difference and t' are directly linked. Pavarini *et al.* pointed out that the maximal T_c in each family of cuprate materials scales with the next nearest hopping t' .⁴ The energy of the Cu $4s$ orbital relative to the pd - σ^* band largely determines t' as the hybridization with the planar oxygen orbitals allows electrons to more effectively hop between $2p_{x,y}$ orbitals. Strong apical $2p_z$ - $4s$ hybridization, determined by the Madelung energy difference, raises the energy of the $4s$ orbital relative to the pd band, reducing the effective hopping t' . Thus, the further away the apical oxygen is located from the CuO_2 plane the larger t' .⁴ Similar empirical relations between T_c and structural details can also be found. For example, there is an optimal distance between the apical oxygen site and the mirror plane of the unit cell for which T_c takes on its maximum value, as shown in Fig. 1. However, despite these observations, a direct connection between changes in the bandstructure and the pairing mechanism is lack-

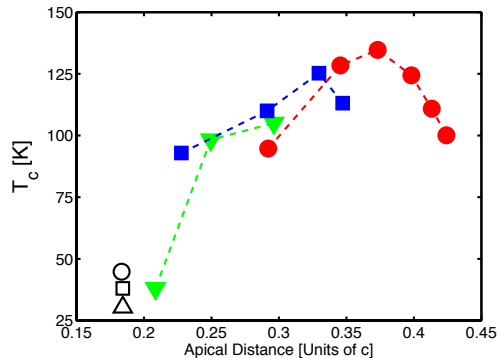


FIG. 1: (Color online) The T_c at optimal doping for many cuprate superconductors plotted as a function of the distance between the apical oxygen site and the mirror plane located at the center of the unit cell. The Hg- (red) circles, Tl- (blue) squares and Bi-families (green) triangles are shown as well as some LSCO and LBCO systems open (black).

ing and to date, the connection between T_c and these c -axis effects remains an empirical intrigue lacking a firm microscopic understanding.

A phonon mechanism has also been pursued since the discovery of HTSC.¹⁹ The original intuition by Bednorz and Müller was that the Jahn-Teller (JT) effect with high-frequency oxygen phonon modes leads to HTSC.²⁰ However, the degeneracy of the two e_g orbitals is lifted considerably (~ 1 eV) and the JT effect is now believed to be ineffective. Furthermore, there are several experiments suggesting a minor role played by phonons. These include the small isotope effect on T_c at optimal doping,²¹ the absence of the phonon effect on the temperature dependence of the resistivity,² and the absence of the phonon bottle-neck effect.²² This conclusion was also supported by early density functional calculations which did not give appreciably high values of couplings and did not support a high T_c in a BCS picture.^{23,24}

The high- T_c cuprates, as strongly correlated systems, have attracted a great deal of theoretical interest.^{25–41} Part of this interest has been focused on examining the renormalization of electron-phonon (el-ph) interactions by strong electron-electron (el-el) correlations.^{25–39} For example, studies of the $t - J$ model incorporating an el-ph interaction indicate that polaron crossover may occur at a weaker el-ph coupling strength than in the case of a pure el-ph coupling model.^{31–33} Quantum Monte Carlo treatments of the single-band Hubbard-Holstein model have shown that the renormalized el-ph vertex develops a strong forward scattering peak with no substantial suppression of the el-ph vertex when the Hubbard U is large³⁴ with similar results obtained for the t - J model.^{35,36} However, using slave-boson approaches, the Hubbard model plus el-ph interaction was found to possess no significant forward scattering peak together with an overall suppression of the el-ph vertex at low temperature.³⁷ This same study observed an enhancement in

the el-ph vertex for small \mathbf{q} scattering at high temperature, which was linked to phase separation. Cumulant expansion techniques³⁸ have also found an enhancement of the el-ph vertex for small \mathbf{q} , again interpreted in terms of incipient phase separation when approaching a critical value of U .

The single-band Hubbard-Holstein model has also been studied within dynamical mean field theory (DMFT). In one study²⁶ the effect of the el-ph interaction was to stabilize the insulating state in the vicinity of the density-driven Mott transition. In a paramagnetic DMFT study²⁸ the el-ph interaction was found to have little effect on the low energy physics produced by the Hubbard interaction while modifying the spectral weight associated with the upper and lower Hubbard bands at higher energy. From these results it was concluded that the primary effect of the el-ph interaction was to reduce the effective value of U . Later work²⁹ considered antiferromagnetic solutions in the presence of el-ph coupling and observed different behavior with strong polaronic effects. In this case, the critical coupling for polaron formation was observed to shift to larger values as the system was doped away from half-filling. The dichotomy between the paramagnetic and antiferromagnetic treatments^{28,29} indicates the possible importance of the magnetic order in considering the el-ph interaction in correlated systems. Finally, a DMFT study invoking a Lang-Firsov transformation for the lattice degrees of freedom has found evidence for a competition between the Mott insulating (metallic) and bipolaronic insulating phases near (away from) half-filling.³⁰

Using the dynamical cluster approximation, an extension of DMFT, examinations of the el-ph interaction within small Hubbard clusters³⁹ find an overall suppression of d -wave superconducting T_c with increasing el-ph coupling. This occurs despite an increase in the apparent pairing correlations within the $d_{x^2-y^2}$ channel. The reduction in T_c was attributed to polaron formation, which reduces quasi-particle weight at the Fermi level and suppresses T_c through the loss of carrier mobility. The enhancement of pairing correlations reported in Ref. 39 indicates that the bare el-ph vertex has been renormalized in favour of d -wave pairing, consistent with the observations of Ref. 34. Furthermore, exact diagonalization (ED) studies on the t - J model, which include el-ph coupling to buckling and breathing vibrations, also show that the former enhance d -wave pairing while the latter suppress it.²⁵ While these results provide no definitive interpretation of the effect of el-ph coupling in strongly correlated systems, there is strong evidence that whatever impact strong correlations may have, the el-ph interaction may still play a significant role that should not be overlooked in these systems.

From an experimental front, the role of phonons in HTSC has become more prominent in recent years. While long-studied from Raman, infrared, and neutron measurements, recent ARPES and scanning tunneling microscopy (STM) measurements on several

cuprates has reinvigorated the exploration of the role of phonons on HTSC.⁴² Experiments on Bi-2212,^{43–46} $\text{La}_{2-x}\text{Sr}_x\text{CuO}_4$ (LSCO),⁴⁷ $\text{Bi}_2\text{Sr}_2\text{CuO}_{6+\delta}$ (Bi-2201),⁴⁸ $\text{Ba}_2\text{Ca}_3\text{Cu}_4\text{O}_8\text{F}_2$,⁴⁹ and Tl families $\text{Tl}_2\text{Ba}_2\text{CaCu}_2\text{O}_8$ (Tl-2212), $\text{TlBa}_2\text{Ca}_2\text{Cu}_3\text{O}_9$ (Tl-1223), and $\text{Tl}_2\text{Ba}_2\text{CuO}_6$ (Tl-2201)⁵⁰ have revealed kinks in the energy dispersion of these materials. These kinks have been interpreted as Hubbard renormalizations,⁵¹ coupling to the neutron resonance and/or spin continuum,⁵² and Engelsberg-Schrieffer renormalizations⁵³ due to coupling of electrons to a collection of optical phonons. These phonons include the out-of-phase c -axis oxygen buckling modes and the in-plane Cu-O bond-stretching modes. The dispersion kink observed in the nodal region, $(0, 0) - (\pi/a, \pi/a)$, and the peak-dip-hump structure observed in the antinodal region, $(0, \pi/a) - (\pi/a, \pi/a)$, clearly shows that the electrons are interacting with bosons of a well defined energy ~ 70 and ~ 36 meV, respectively. For the nodal region, it has been convincingly argued that this structure is due to the oxygen bond-stretching phonon as the kink is observed independent of superconductivity and of the presence/absence of the spin resonance peak. As for the anti-nodal region, it has been claimed that the kink appears only below T_c , and hence it is attributed to the spin resonance mode at 41 meV.⁵⁴ However, an extensive study conducted more recently has found the evidence for the kink structure in the normal state and over a wide range of momentum space.⁴⁴ Further, contrasting single and multilayer cuprate “kinks”, and materials known to have a neutron resonance, also indicates that the observed renormalizations are most likely due to optical phonons, although this is still controversial.^{50,55,56}

It is well known that the c -axis phonons show some of the most dramatic lineshape changes with doping and temperature compared to any phonons observed via neutron⁵⁷ and Raman⁵⁸ scattering. For example, the apical phonon frequency shifts by as much as 20 cm^{-1} with doping and temperature in a number of compounds: $\text{La}_{2-x}\text{Sr}_x\text{CuO}_4$, $\text{HgBa}_2\text{Ca}_{n-1}\text{Cu}_n\text{O}_{4n+\delta}$ ($n = 1 - 4$) and $\text{Bi}_2\text{Sr}_2\text{Ca}_2\text{Cu}_3\text{O}_{10+\delta}$.^{57,58} Moreover, recent ARPES data on Bi-2201 have shown kinks in the energy range of the c -axis phonons which are weaker in overdoped compounds in comparison to optimal doped compounds.⁴⁸ This has also been interpreted in terms of increased screening of the el-ph interaction with increasing hole concentrations. In addition, the anomaly of the Raman A_{1g} -polarized mode due to the onset of superconductivity is observed in three- and four-layer compounds.⁵⁹ This has been successfully analyzed in terms of the internal electric field produced by the interlayer Josephson plasmon and its coupling to the phonon. This means that the system behaves as an ionic crystal along the c -axis in the normal state, and suddenly turns into a superconductor.

While the role of the neutron resonance and phonons remains controversial, it is of relevant interest whether these signatures in ARPES may be used as an angle-resolved analogy to the tunnelling ripples in conventional superconductors,⁶⁰ thus providing information on the

pairing mechanism in the cuprates. In order to connect el-ph coupling to a possible pairing mechanism a systematic study of coupling across families of cuprate materials is desirable. In Ref. 61 ARPES observed renormalizations of the band were interpreted as due to the B_{1g} branch for anti-nodal electrons and the bond-stretching branch for nodal electrons. While the latter coupling is of a deformation type, the coupling constructed for the B_{1g} branch involves a charge-transfer between planar oxygens due to a modulation of the electrostatic or Madelung energies of the planar oxygen sites. A local crystal field, generated by a mirror plane symmetry breaking, allows for a coupling at first order in atomic displacements.⁶² (We note here that the A_{1g}/B_{1g} nomenclature only holds for Raman $\mathbf{q} = 0$ momentum transfers. However, throughout this work we denote the entire out-of-phase branch as “ B_{1g} ” and the entire in-phase branch as “ A_{1g} ”.) Since the cuprates are poor conductors along the c -axis, the electrostatic interaction can be thought to be largely unscreened. Calculations based on Ewald’s method have been performed on $\text{YBa}_2\text{Cu}_3\text{O}_7$ (YBCO)⁶³ and large crystal fields have been obtained and the resulting coupling matches well with the coupling determined from Fano lineshape analysis of Raman data.⁶²

Recently, the issue of whether the el-ph coupling in the cuprates is strong enough to explain the observed band renormalizations has been revisited via density functional (LDA) calculations,^{64–66} updating previous estimates.^{23,24} While many efforts have been made to extract bosonic coupling from ARPES renormalizations in the cuprates, there is no widely accepted way to uniquely determine the strength of the coupling at kink energies, and thus reliable comparisons of calculations with experiment must be viewed with some caution.⁶⁷ While LDA calculations have provided remarkably good agreement with phonon dispersions, there are a number of facets of LDA calculations which may only provide part of the story of el-ph coupling. As LDA calculations overestimate the itinerancy of the electrons, they describe the cuprates as good metals even at half-filling. Moreover, the obtained interlayer transfer integral and hence the c -axis plasmon frequency is both coherent and much larger than the experimental observation. Both of these factors serve to overestimate the screening ability of the cuprates, especially in the underdoped region, and thus underestimates the strength of the el-ph interaction. This may be one of the reasons why LDA predicts smaller linewidths for the half-breathing oxygen bond-stretching modes and the apical oxygen modes, sometimes by more than one order of magnitude.⁶⁸ It is therefore not clear if these findings indicate that the el-ph coupling is small or that DFT-based approaches alone are inadequate for describing the physics of the cuprates. As has been found in STM experiments,¹¹ a nano-scale inhomogeneous structure on a length scale of 15 \AA exists universally in Bi-2212 and YBCO. This length scale cannot be larger than the screening length and we can conclude that the screening length within the CuO_2 plane is not shorter than 15 \AA ,

much longer than the Thomas-Fermi screening length of the typical metal ($\sim 0.5 \text{ \AA}$). Furthermore, charge transfer between the layers is almost prohibited. As a result of the transfer integral between the layer is proportional to $[\cos(k_x a) - \cos(k_y a)]^2$, the opening of the pseudogap in the $(\pi, 0)$ and $(0, \pi)$ regions strongly suppresses the inter-layer hopping. Considering these discrepancies between LDA and experiments, one can imagine that the el-ph coupling is in reality much stronger than LDA predicts. Focusing on the buckling modes, theoretical consideration have been limited to the two-dimensional plane and the inter-layer Coulomb interaction has been neglected. This is usually justified in the metal since the screening length is much shorter than the interlayer distance. This is not the case in the cuprates.

In this paper we provide a comprehensive and self-contained story on el-ph coupling to oxygen phonons as a function of doping across the cuprate families. We formulate a theory for el-ph coupling in the cuprates taking into account the local environment around the CuO_2 planes, the poor screening of charge fluctuations out of the plane, doping-dependent band character variations, and structural differences across the cuprate superconductors.

The organization of this paper is as follows. In section II we present a general discussion of el-ph coupling to c -axis oxygen phonons. After summarizing prior work on the out-of-plane planar oxygen modes, we then provide a derivation of the coupling to modes involving c -axis apical oxygen motion. In section III we then discuss the anisotropy of the bare couplings and examine the total strength of the bare el-ph coupling and its contribution to the single-particle self-energy and d -wave anomalous self-energy.

In section IV we develop the formalism for poor screening and examine its implications for the anisotropy and overall magnitude of the renormalized el-ph vertices. Due to the poor c -axis conductivity we find that the c -axis phonons cannot be effectively screened for small in-plane momentum transfer \mathbf{q}_{2D} . This effect becomes more pronounced as the crystal becomes more ionic and screening becomes increasingly inoperable in the underdoped side of the phase diagram. However, in the case of the B_{1g} modes the coupling is anomalously anti-screened producing an enhancement of the coupling in the anti-nodal region. In terms the projected d -wave couplings, the small \mathbf{q}_{2D} behavior of the screened vertices produces an enhancement in the total phonon contribution to pairing. Therefore, the combined effects of poor screening reduces the total el-ph coupling and enhances the d -wave projected coupling with doping. This has important implications for the doping dependence of the el-ph self-energies probed by ARPES as well as any contribution to pairing mediated by phonons.

In section V we turn to materials trends and a systematic examination of the Madelung potential and crystal field strengths across the Bi-, Tl- and Hg families of cuprates is presented. Here, using an ionic point charge

model and the Ewald summation technique, we identify systematic trends in the strength of the crystal fields which mirror trends in the material's T_c at optimal doping. Through this observation we link the structure and chemical composition to the strength of the coupling to the c -axis modes and discuss how this can be used to understand the large variations in T_c observed across the cuprates. We also present considerations for doping-induced changes to the value of the crystal field in Bi-2212.

In light of these findings, section VI presents a simple two-channel model for pairing in the cuprates, which includes a dominant, d -wave pairing, high-energy bosonic mode and a weaker phonon mode. Using this model, we demonstrate that phonons can provide a sizeable enhancement to T_c which is in excess of the T_c that would be obtained from phonons alone. Furthermore, due to the dominant bosonic mode, the resulting value of the isotope exponent α is small ($\alpha < 0.15$) despite the large enhancement of T_c (~ 40 K). This calculation, in combination with the materials and doping dependent trends identified in the previous sections, shows that a phonon assisted pairing model provides a natural framework for understanding trends observed for T_c across the cuprates. Finally, in section VII we conclude by summarizing our findings and discuss open questions concerning el-ph coupling in strongly correlated systems.

In addition to the treatment outline above, in the appendix we explore how el-ph coupling to c -axis modes is modified by strong correlations in the half-filled parent insulators using exact diagonalization of small multi-band Hubbard clusters. Specifically we address how el-ph coupling modifies the properties of the Zhang-Rice singlet (ZRS). Here we find that static lattice displacements have a strong influence on the ZRS hoppings, energy and antiferromagnetic exchange energy J . These results have a direct impact on the use of down-folded models such as the t - J model as they indicate that the effects of the el-ph coupling cannot be simply cast as modulations of a single parameter such as t , J , or the energy of the ZRS.

II. GENERAL ELECTRON-PHONON CONSIDERATIONS IN THE CUPRATES

In this section we present a review of some generic considerations for electrons coupling to oxygen motions in and out- of the CuO_2 plane. Since many of the derivations have appeared before, we can be brief, with the main aim to generalize previous results to a five band model in order to include off-axis orbitals and apical oxygen phonon modes.

We begin by considering an ideal CuO_2 plane isolated from its environment. Since hopping integrals are modulated to second order in atomic displacements along the c -axis, the el-ph coupling due to this mechanism is weak. However, if the same plane is placed in an asymmetric electrostatic environment a local crystal field, which

breaks mirror plane symmetry, provides a coupling linear in displacement. The plane must then spontaneously buckle in a pattern where the oxygen (copper) atoms are displaced away from (towards) the mirror plane.

In a three band model,⁶² the local field coupling was used to construct a charge-transfer el-ph vertex for coupling to the Raman active out-of-phase and in-phase c -axis oxygen vibrations. The in-phase phonon modulates charge transfer between planar oxygen and copper orbitals while the out-of-phase phonon modulates charge transfer between only the planar oxygen orbitals. A single-band el-ph coupling was obtained:

$$H_{el-ph} = \frac{1}{\sqrt{N}} \sum_{\mathbf{k}, \mathbf{q}, \sigma} |g(\mathbf{k}, \mathbf{q})|^2 c_{\mathbf{k}-\mathbf{q}, \sigma}^\dagger c_{\mathbf{k}, \sigma} [b_{\mathbf{q}}^\dagger + b_{-\mathbf{q}}], \quad (1)$$

where $c_{\mathbf{k}, \sigma}^\dagger$ ($c_{\mathbf{k}, \sigma}$) creates (annihilates) an electron in the partially filled antibonding band with momentum \mathbf{k} , energy $\epsilon_{\mathbf{k}}$, and spin σ , and $b_{\mathbf{q}}^\dagger$ ($b_{\mathbf{q}}$) creates (annihilates) a phonon of energy $\Omega_{\mathbf{q}}$ and wavevector \mathbf{q} .

Considering a modulation of the electrostatic coupling of the charge density at the oxygen sites coupled to the local on-site potential Φ_{ext} , the Hamiltonian is of the form⁶²

$$H'_{site} = -e \sum_{\mathbf{n}, \sigma} p_{\mathbf{n}, \sigma}^\dagger p_{\mathbf{n}, \sigma} \Phi_{ext}[\mathbf{u}(\mathbf{a}\mathbf{n})], \quad (2)$$

where $\mathbf{u}(\mathbf{a}\mathbf{n})$ is the oxygen displacement vector in the unit cell at lattice site \mathbf{n} , e is the electron charge and $p_{\mathbf{n}, \sigma}^\dagger$ ($p_{\mathbf{n}, \sigma}$) creates (annihilates) an electron at site \mathbf{n} , which can include both planar and apical oxygen orbitals. This coupling mechanism differs from the deformation coupling considered in Ref. 24. Expanding for small displacements $H'_{site} = H_{site} + H_{el-ph} + O(u^2)$ where H_{site} includes the Madelung contribution to the site energies and the term linear in \mathbf{u} generates the el-ph interaction

$$H_{el-ph} = -e \sum_{\mathbf{n}, \sigma} p_{\mathbf{n}, \sigma}^\dagger p_{\mathbf{n}, \sigma} \mathbf{E}_{\mathbf{n}} \cdot \mathbf{u}(\mathbf{a}\mathbf{n}). \quad (3)$$

$\mathbf{E}_{\mathbf{n}}$ is the local crystal field at the oxygen site provided this field is finite, which occurs at locations of broken mirror symmetry in the unit cell.

In order to derive the form of the coupling $g(\mathbf{k}, \mathbf{q})$ Eq. (3) must be rewritten in the form of Eq. (1). To do so, the el-ph Hamiltonian is Fourier transformed to momentum space and the oxygen operators are replaced by band representation operators $p_{\mathbf{k}, \delta, \sigma} = \phi_\delta(\mathbf{k}) c_{\mathbf{k}, \sigma}$. Here, $\phi_\delta(\mathbf{k})$ is the oxygen ($\delta = x, y$ for planar oxygen and $\delta = a$ for apical oxygen) eigenfunction for the $pd\text{-}\sigma^*$ band, which is obtained from a tight-binding model for the CuO_2 plane.

A. Multi-band Models

Prior work focusing on the A_{1g} , B_{1g} and breathing branches made use of a three-band model.^{15,61,62} In order to extend these works to include the apical oxygen

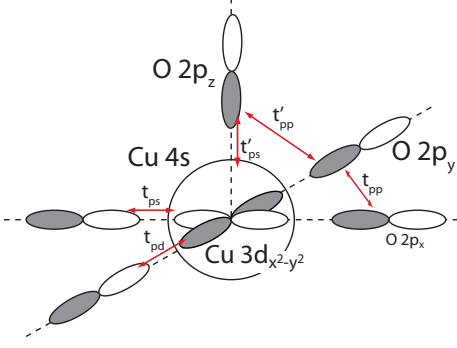


FIG. 2: (Color online) The five-band model used to derive the form of the el-ph couplings $g(\mathbf{k}, \mathbf{q})$.

modes this model must be extended to a five-band model as shown in Fig. 2. The basis set of this model contains a $4s$ ($s_{\mathbf{n},\sigma}, s_{\mathbf{n},\sigma}^\dagger$) and $3d_{x^2-y^2}$ ($d_{\mathbf{n},\sigma}, d_{\mathbf{n},\sigma}^\dagger$) orbital on each copper site \mathbf{n} , two planar oxygen $2p_{x,y}$ orbitals ($p_{\mathbf{n},\delta,\sigma}, p_{\mathbf{n},\delta,\sigma}^\dagger$) with $\delta = x, y$, and one apical oxygen $2p_z$ orbital ($a_{\mathbf{n},\sigma}, a_{\mathbf{n},\sigma}^\dagger$). Here, we neglect the in-plane O $2p$ orbitals oriented perpendicular to the Cu-O bonds. These orbitals form weaker pd - π bonds with the lower energy Cu t_{2g} orbitals and do not contribute heavily to the character of the band crossing the fermi level.²⁴ Site energies are denoted by $\epsilon_{s,d,p,z}$, respectively. Defining canonical fermions⁶⁹ α, β from combinations of the planar oxygen orbitals via a Wannier transformation

$$\alpha_{\mathbf{k},\sigma}, \beta_{\mathbf{k},\sigma} = \pm i \frac{s_{x,y}(\mathbf{k}) p_{\mathbf{k},x,\sigma} \mp s_{y,x}(\mathbf{k}) p_{\mathbf{k},y,\sigma}}{\mu_{\mathbf{k}}}, \quad (4)$$

where $s_{x,y} = \sin(k_{x,y}a/2)$ and $\mu_{\mathbf{k}}^2 = s_x^2(\mathbf{k}) + s_y^2(\mathbf{k})$, the Hamiltonian can be written as $H = \sum_{\mathbf{k},\sigma} H_{\mathbf{k},\sigma}$:

$$\begin{aligned} H_{\mathbf{k},\sigma} = & H_{site} - 2t_{pp}\nu_{\mathbf{k}}[\beta_{\mathbf{k},\sigma}^\dagger\beta_{\mathbf{k},\sigma} - \alpha_{\mathbf{k},\sigma}^\dagger\alpha_{\mathbf{k},\sigma}] \\ & + 2 \left[t_{pd}\mu_{\mathbf{k},\sigma} d_{\mathbf{k},\sigma}^\dagger \alpha_{\mathbf{k},\sigma} + t_{pp}\chi_{\mathbf{k}} \alpha_{\mathbf{k},\sigma}^\dagger \beta_{\mathbf{k},\sigma} \right. \\ & + t_{ps}\kappa_{\mathbf{k}} s_{\mathbf{k},\sigma}^\dagger \alpha_{\mathbf{k},\sigma} - t_{ps}\lambda_{\mathbf{k}} s_{\mathbf{k},\sigma}^\dagger \beta_{\mathbf{k},\sigma} + \frac{t'_{ps}}{2} s_{\mathbf{k},\sigma}^\dagger a_{\mathbf{k},\sigma} \\ & \left. - t'_{pp}\kappa_{\mathbf{k}} a_{\mathbf{k},\sigma}^\dagger \alpha_{\mathbf{k},\sigma} + t'_{pp}\lambda_{\mathbf{k}} a_{\mathbf{k},\sigma}^\dagger \beta_{\mathbf{k},\sigma} + h.c. \right] \quad (5) \end{aligned}$$

with H_{site} containing the site energies and $h.c.$ denoting the hermitian conjugate. Finally, the basis functions are defined as:

$$\begin{aligned} \nu_{\mathbf{k}} &= 4 \frac{s_x^2(\mathbf{k})s_y^2(\mathbf{k})}{\mu_{\mathbf{k}}^2} & \kappa_{\mathbf{k}} &= \frac{s_x^2(\mathbf{k}) - s_y^2(\mathbf{k})}{\mu_{\mathbf{k}}} \\ \lambda_{\mathbf{k}} &= 2 \frac{s_x(\mathbf{k})s_y(\mathbf{k})}{\mu_{\mathbf{k}}} & \chi_{\mathbf{k}} &= \lambda_{\mathbf{k}}\kappa_{\mathbf{k}}. \quad (6) \end{aligned}$$

In the limit where the apical and copper $4s$ orbitals are removed ($t_{ps} = t'_{ps} = 0$, etc.) there expressions recover prior work carried out using a three-band model.^{15,61,62}

B. Planar Oxygen c -Axis Modes

For planar oxygen vibrations the el-ph coupling is given by ($\mathbf{p} = \mathbf{k} - \mathbf{q}$)

$$\begin{aligned} g_{B_{1g}, A_{1g}}(\mathbf{k}, \mathbf{q}) = & eE_z \sqrt{\frac{\hbar}{2M_O N(\mathbf{q}) \Omega_{B_{1g}, A_{1g}}}} \\ & \times \left[\phi_x^\dagger(\mathbf{k}) \phi_x(\mathbf{p}) e^{-iq_x a/2} (1 + e^{-iq_y q}) \mp \right. \\ & \left. \phi_y^\dagger(\mathbf{k}) \phi_y(\mathbf{p}) e^{-iq_y a/2} (1 + e^{-iq_x a}) \right] \quad (7) \end{aligned}$$

where the minus (plus) sign is for coupling to the B_{1g} (A_{1g}) branch. Here M_O denotes the oxygen mass, E_z is the c -axis component of the local field at the planar oxygen site, $N^2(\mathbf{q}) = 4[\cos^2(q_x a/2) + \cos^2(q_y a/2)]$ is the phonon eigenvector normalization, and $\Omega_{A_{1g}, B_{1g}}$ denote the assumed dispersionless frequencies of the B_{1g} and A_{1g} branches, respectively. The motion of the heavier Cu atoms has been neglected in this treatment. Eq. (7) is a generic expression for the A_{1g} and B_{1g} vertices, independent of the underlying tightbinding model used to determine the band eigenfunctions $\phi_{x,y,Cu}(\mathbf{k})$. In the three-band model, the band eigenfunctions are defined as⁶¹

$$\begin{aligned} \phi_{x,y}(\mathbf{k}) &= \mp \frac{i}{A(\mathbf{k})} [\epsilon(\mathbf{k}) t_{x,y}(\mathbf{k}) - t'(\mathbf{k}) t_{y,x}(\mathbf{k})] \\ \phi_{Cu}(\mathbf{k}) &= \frac{1}{A(\mathbf{k})} [\epsilon^2(\mathbf{k}) - t^2(\mathbf{k})], \quad (8) \end{aligned}$$

where $t_{x,y}(\mathbf{k}) = t_{pd} s_{x,y}(\mathbf{k})$, $t'(\mathbf{k}) = -4t_{pp} \sin_x(\mathbf{k}) \sin_y(\mathbf{k})$, the normalization is

$$\begin{aligned} A^2(\mathbf{k}) = & [\epsilon^2(\mathbf{k}) - t^2(\mathbf{k})]^2 + [\epsilon(\mathbf{k}) t_x(\mathbf{k}) - t'(\mathbf{k}) t_y(\mathbf{k})]^2 \\ & + [\epsilon(\mathbf{k}) t_y(\mathbf{k}) - t'(\mathbf{k}) t_x(\mathbf{k})]^2, \quad (9) \end{aligned}$$

and $\epsilon(\mathbf{k})$ is the bare dispersion, given in Ref. 62. From Eq. (7) it can be seen that the symmetry of the phonon is implanted into the el-ph coupling to provide substantial momentum anisotropy. For the B_{1g} phonon branch, $g(\mathbf{k}, \mathbf{q})$ changes sign for $k_x, q_x \rightarrow k_y, q_y$, while for the A_{1g} phonon branch it does not. As a result the coupling involves all fermionic states for the A_{1g} branch, while for the B_{1g} branch the antinodal states along the Brillouin zone (BZ) axes are weighted heavily and nodal states along the zone diagonal are projected away.

C. Apical Oxygen c -Axis Modes

Since apical phonons show some of the strongest renormalizations in La- and Hg-cuprates,^{57,58} and since the apical oxygen atoms do not lie in a mirror plane symmetry even in single layer cuprates, they are included as an extension of our previous work. Early on the apical phonon was thought to be quite anharmonic and related

to the Jahn-Teller mechanism in $\text{YBa}_2\text{Cu}_3\text{O}_7$,⁷⁰ although many confusing results were found.⁷¹ More recently the coupling is thought to be electrostatic^{72,73} in nature and in some treatments weakly momentum dependent.⁷² It should be emphasized that formally a Holstein (momentum independent) coupling in any model with long-range Coulomb interactions will be screened out by backflow due to charge conservation and therefore the coupling is expected to be very small. This will be discussed in Section IV. Here instead we place focus on a strongly momentum dependent coupling arising from charge transfer mechanisms between apical and planar oxygen orbitals, similar to the electronic pathways involved in c -axis tunnelling.⁷⁴

An apical orbital displacement modulates the Madelung energy as in Eq. (3) and the resulting el-ph coupling is of the form of Eq. (1), with

$$g_{apex}(\mathbf{k}, \mathbf{q}) = g_0^{apex} \phi_a^\dagger(\mathbf{k}) \phi_a(\mathbf{k} - \mathbf{q}) \epsilon_a^z(\mathbf{q}). \quad (10)$$

Here, $\epsilon_a^z(\mathbf{q})$ is the c -axis component of the eigenvector for the apical branch coming from the atomic displacement in Eq. (3), $g_0^{apex} = eE_z^a \sqrt{\hbar/2M_O\Omega_a}$, and $\phi_a(\mathbf{k})$ is the apical eigenfunction, obtained from diagonalizing Eq. (5). For our purpose however, we are primarily interested in the leading order momentum dependence of the coupling $g(\mathbf{k}, \mathbf{q})$. Starting from Eq. (5), the Löwdin

down-folding procedure⁷⁵ is applied to determine the apical character of the resulting partially filled band crossing the Fermi level. The resulting form for the apical eigenfunction $\phi_a(\mathbf{k})$ is then

$$\phi_a(\mathbf{k}) = 2t_{pz} \frac{\kappa_{\mathbf{k}}}{\epsilon_{\mathbf{k}} - \epsilon_a}$$

with $\kappa_{\mathbf{k}}$ defined in Eq. (6). Finally, for simplicity we neglect the momentum dependence of the apical phonon's eigenvector and set $\epsilon_a^z(\mathbf{q}) = 1$. More complicated models in which the apical phonon involves the motion of the in-plane oxygens can be treated accordingly.

The local crystal field E_z^a at the apical oxygen site modulates a charge transfer between the apical oxygen and the planar orbitals. This mechanism of charge transfer is analogous to the charge transfer mechanism yielding bi-layer splitting.⁷⁴ From Eqs. (5) and (10), the resulting momentum dependence of the coupling via this transfer, $g(\mathbf{k}, \mathbf{q}) \sim [\cos(k_x a) - \cos(k_y a)][\cos(p_x a) - \cos(p_y a)]$ with $\mathbf{p} = \mathbf{k} - \mathbf{q}$, is strongest for anti-nodal electrons, and has a form factor similar to c -axis hopping $t_\perp(\mathbf{k})$.⁷⁴ Although this coupling has an anisotropy similar to that of the coupling to the B_{1g} branch, it does not contribute to d -wave pairing due to its phase and momentum dependence at large q .

D. In-plane Bond-Stretching Modes

For completeness, we also consider the coupling to the planar Cu-O bond stretching modes, the so-called breathing modes, within the framework of the three-band model, as derived in Refs. 32, 36 and 61. The bond-stretching modes couple to electrons via both a direct modulation of the hopping integral t_{pd} as well as electrostatic changes in the Madelung energies as the orbitals are displaced.³⁶ As done in Ref. 32 we consider only the overlap modulation. The derivation is briefly sketched here.

To obtain the form of the el-ph coupling the overlap integral t_{pd} is taken to be site dependent $t_{pd}^{\mathbf{n}}$. It is then assumed that the Cu and O atomic displacements, $\mathbf{u}_{\mathbf{n}}^{Cu}$ and $\mathbf{u}_{\mathbf{n},\alpha}^O$, about their equilibrium positions, $R_{\mathbf{n}}$ and $R_{\mathbf{n}} + \hat{\delta}a/2$, where $\hat{\delta}$ are basis vectors for the CuO_2 plane, are small. The overlap integral is expanded and only the first order term is retained

$$t_{pd}^{\mathbf{n}} = t_{pd}^0 + \sum_{\delta=\pm\hat{x},\pm\hat{y}} \vec{\nabla} t_{pd}^{\mathbf{n}}|_{r=R_{\mathbf{n}}} \cdot \left(\mathbf{u}_{\mathbf{n}}^{Cu} - \mathbf{u}_{\mathbf{n}+a\hat{\delta}/2}^O \right) + O(u^2) \quad (11)$$

The modulation of the hopping integrals provides the el-ph coupling Hamiltonian

$$H_{el-ph}^{br} = \sum_{n,\sigma,\delta} P_\delta \vec{\nabla} t_{pd}^{\mathbf{n}}|_{r=R_{\mathbf{n}}} \cdot \left[\mathbf{u}_{\mathbf{n}}^{Cu} - \mathbf{u}_{\mathbf{n}+a\hat{\delta}/2}^O \right] \left[d_{n,\sigma}^\dagger p_{n,\sigma,\delta} + h.c. \right], \quad (12)$$

with $P_{x,y} = \pm 1 = -P_{-x,-y}$ denoting the phase of the Cu-O overlap. Following Ref. 61, we neglect the Cu vibration and set $\partial t_{pd}^{\mathbf{n}}/\partial x|_{R_{\mathbf{n}}} = -Q_\delta g_{dp}$, where $Q_{\pm x} = Q_{\pm y} = \pm 1$ and g_{dp} is a scalar function that depends on the equilibrium Cu-O distance. The el-ph coupling Hamiltonian can then be simplified to

$$H_{el-ph}^{br} = g_{dp} \sum_{n,\delta,\sigma} P_\delta Q_\delta u_\delta^O(n) \left[d_{n,\sigma}^\dagger p_{n,\sigma,\delta} + h.c. \right], \quad (13)$$

as obtained in Ref. 61. Here u_δ^O denotes the displacement of the oxygen atom δ along the Cu-O bond. By introducing the Fourier transform the el-ph coupling may be re-written as:

$$H_{el-ph}^{br} = \frac{g_0^{br}}{\sqrt{N}} \sum_{\mathbf{k}, \mathbf{q}} \sum_{\sigma, \delta=x,y} P_\delta \cos(k_\alpha a/2) \epsilon_\delta^O(\mathbf{q}) [d_{\mathbf{k}, \sigma}^\dagger p_{\mathbf{k}-\mathbf{q}, \sigma, \delta} + p_{\mathbf{k}+\mathbf{q}, \sigma, \delta}^\dagger d_{\mathbf{k}, \sigma}] (b_{\mathbf{q}}^\dagger + b_{-\mathbf{q}}). \quad (14)$$

Here, $\epsilon_\delta(\mathbf{q}) = \sin(q_\delta a/2) / \sqrt{\sin^2(q_x a/2) + \sin^2(q_y a/2)}$ is the component of the phonon eigenvector for oxygen δ parallel to the Cu-O bond. Finally, the electronic eigenfunctions of the planar O $\phi_{x,y}(\mathbf{k})$ and Cu $3d_x^2 - y^2$ orbitals $\phi_{Cu}(\mathbf{k})$ for the pd- σ^* band, with operators c, c^\dagger , are introduced. The resulting Hamiltonian reduces to the form of Eq. (3) with

$$g_{br}(\mathbf{k}, \mathbf{q}) = g_0^{br} \sum_{\alpha=x,y} P_\alpha \epsilon_\alpha(\mathbf{q}) [\cos(p_\alpha a/2) \phi_{Cu}(\mathbf{p}) \phi_\alpha(\mathbf{k}) - \cos(k_\alpha a/2) \phi_{Cu}(\mathbf{k}) \phi_\alpha(\mathbf{p})] \quad (15)$$

Here $\mathbf{p} = \mathbf{k} - \mathbf{q}$, $g_0^{br} = g_{dp} \sqrt{\hbar/2M_O \Omega_{\mathbf{q}}}$. We note that generally $t_{pd}(d_{Cu-O}) \sim d_{Cu-O}^\beta$ and thus $g_{pd} = \beta t_{pd}/d_{Cu-O}$. Since typically $\beta = 3.5$,³² an estimate for the strength of the coupling is obtained from $g_{pd} \sim 2 \text{ eV}/\text{\AA}$ for $t_{pd} = 1.1 \text{ eV}$. For $\Omega_{\mathbf{q}} = 70 \text{ meV}$, this gives $g_{br} = 86 \text{ meV}$.

III. K,Q-MOMENTUM DEPENDENCE OF THE BARE VERTICES

A. Momentum dependence throughout the Brillouin Zone

In the previous section it was shown how the explicit form for el-ph coupling to oxygen modes is determined by the nature of the charge transfer modulated by the lattice displacement, the local environment surrounding the CuO₂ plane, as well as the orbital content of a single downfolded band crossing the Fermi level. The relevant parameters - magnitude of orbital hybridization, local crystal field, the charge-transfer energy, the shape of the Fermi surface, and the density of states at the Fermi level - all contribute in setting the overall magnitude of the coupling as well as the full fermionic \mathbf{k} and bosonic \mathbf{q} momentum dependence of the coupling $g(\mathbf{k}, \mathbf{q})$. The band character enters through the band eigenvectors ϕ which further depend on the complexity of the unit cell. At the BZ center the wavefunctions are atomic and the character of the band is unique. Large momentum variations of the band character then occur for increasing momentum, and a very strong momentum dependence of the overall el-ph coupling can occur. This strong momentum dependence has indeed been observed in recent LDA treatments⁶⁴.

We remark that we are first interested in the magnitude and anisotropy of the bare couplings in the absence of charge screening in order to determine possible discrepancies with LDA treatments, which treat correlations on the mean field level and give 3D metallic screening. In order to estimate general tendencies, momentum dependencies as well as magnitudes, in this section we explore some simplifications.

We begin by assuming that $2t_{pd}$ is much greater than any relevant energy scale in the system, keeping in mind that the charge transfer energy $\Delta = \epsilon_p - \epsilon_d \sim 0.8 \text{ eV}$ is much reduced from its bare value $\sim 3.5 \text{ eV}$ when treating correlations in mean field approaches like LDA.²⁴ In this limit the ϕ functions can be represented as

$$\phi_{x,y}(\mathbf{k}) = \pm i \frac{\sin(k_{x,y} a/2)}{\sqrt{\sin^2(k_x a/2) + \sin^2(k_y a/2)}} + O(\Delta/2t_{pd})^2$$

and

$$\phi_{Cu} = \frac{\Delta/2t_{pd}}{\sqrt{\sin^2(k_x a/2) + \sin^2(k_y a/2)}}.$$

To the same order, the denominators in these expressions are constant over constant energy contours. Therefore, since we will restrict ourselves largely to the Fermi surface, we represent the band functions $\phi_{x,y}(\mathbf{k}) = A_O \sin(k_\alpha a/2)$, $\phi_b(\mathbf{k}) = A_{Cu}$ and $\phi_a(\mathbf{k}) = A_a d_k$, with $d_k = [\cos(k_x a/2) - \cos(k_y a/2)]/2$ and the coefficients determined by $A_O^2 = \langle \phi_{x,y}^2(\mathbf{k}) \rangle / \langle \sin^2(k_{x,y} a/2) \rangle$, $A_{Cu}^2 = \langle \phi_b^2(\mathbf{k}) \rangle$ and $A_a^2 = \langle \phi_a^2(\mathbf{k}) \rangle / \langle d_k^2 \rangle$, respectively. Here $\langle \dots \rangle$ denotes a Fermi surface average: $\langle A \rangle = \sum_{\mathbf{k}} A_{\mathbf{k}} \delta(\epsilon_{\mathbf{k}}) / \sum_{\mathbf{k}} \delta(\epsilon_{\mathbf{k}})$. In this way, the overall coupling anisotropy can be simplified without loss of generality.

As a consequence, the fermionic momentum dependence of the coupling to the breathing modes disappears:

$$g_{br}(\mathbf{k}, \mathbf{q}) = g_0^{br} A_{Cu} A_O \sum_{\alpha=x,y} P_\alpha \epsilon_\alpha(\mathbf{q}) \sin(q_\alpha a/2).$$

Substituting the phonon eigenvectors, the coupling to the breathing modes becomes

$$g_{br}(\mathbf{q}) = g_0^{br} A_{Cu} A_O \sqrt{\sin^2(q_x a/2) + \sin^2(q_y a/2)}. \quad (16)$$

This form has also been obtained in a t - J approach³² however, in this case, the oxygen and copper character have been explicitly retained through A_O and A_{Cu} , respectively.⁷⁶

The el-ph vertex for the A_{1g} and B_{1g} modes can be likewise simplified

$$g_{A_{1g}, B_{1g}}(\mathbf{k}, \mathbf{q}) = eE_z \sqrt{\frac{2\hbar}{M_{ON}(\mathbf{q})\Omega_{B_{1g}, A_{1g}}}} A_O^2 e^{-i(q_x+q_y)a/2} \times [\sin(k_x a/2) \sin(p_x a/2) \cos(q_y a/2) \pm \sin(k_y a/2) \sin(p_y a/2) \cos(q_x a/2)] \quad (17)$$

These expressions recover the Raman form factors in the limit $\mathbf{q} \rightarrow 0$ for each mode and they obey the symmetry conditions for momentum reflections about 45° as discussed previously. The fermionic momentum dependence cannot be neglected in either of these expressions, where in particular, a strong fermionic momentum dependence of the coupling to the B_{1g} modes occur, preferentially weighting anti-nodal states with small momentum transfers.

Lastly, the momentum structure of the apical coupling simplifies considerably in the same manner:

$$g_{apex}(\mathbf{k}, \mathbf{q}) = g_o^{apex} A_a^2 [\cos(k_x a) - \cos(k_y a)][\cos(p_x a) - \cos(p_y a)]/4. \quad (18)$$

Once again, a substantial fermionic momentum dependence emerges from the c -axis charge transfer pathways and the apical character of the band.

Before proceeding further a few comments are in order. In using Eqs.(16)-(18) we have simplified the el-ph couplings while explicitly retaining the role of the band character in determining the overall strength of the couplings. Since the eigenfunctions enter to the fourth power for $|g|^2$, the total coupling strengths determined in this approach may change considerably when adjusting multi-band parameters. However, this method has the advantage that the materials dependence of the coupling, parameterized by A_O , A_a and A_{Cu} , can be calculated using a variety of methods such as exact diagonalization, quantum Monte Carlo or LDA. We also emphasize that the total coupling strengths (calculated in the next section) that we obtain using this formalism are similar to those obtained from LDA treatments, even though the latter includes the effects of screening.^{23,64,65}

This approach also allows for the use of a renormalized bandstructure, while retaining the explicit band character of the original five-band model. This is important since the overall strength of the el-ph couplings scales with the density of states at the Fermi level N_F (see Eq. (19)); narrow bandwidth systems will exhibit larger coupling in comparison to large bandwidth systems with the same vertex $g(\mathbf{k}, \mathbf{q})$. With an appropriate choice in parameters, the five-band model given in section II reasonably reproduces the bandwidth (and N_F) determined by LDA calculations.⁷⁷ However, as has been noted,⁶⁸ LDA over predicts the total bandwidth (and consequently N_F is under predicted) in comparison with experiment. Therefore, we expect that the total couplings will be underestimated using the five-band model with parameters chosen to match LDA. A simple rescaling of the five-band model bandstructure in conjunction with the full form of the ϕ -functions is insufficient to correct this since this procedure would produce incorrect values for the ϕ -functions and therefore generate errors in the character of the band as a function of \mathbf{k} . However, the use of the couplings defined by Eqs. (16)-(18) allows us to resolve this issue. Here, the correct band character is captured by calculating A_O , A_{Cu} and A_a using the five-

band model but the Fermi surface and bandstructure are obtained from elsewhere in order to better match experiment. In this work, we adopt a five-parameter tight-binding model for Bi-2212 derived from fits to ARPES data.⁷⁸ This approach allows us to capture the increased value of N_F while simultaneously retaining estimates for the correct band character. We also note that the specific shape of the Fermi surface is not crucial to the overall anisotropy of the couplings.

To visualize the momentum dependence of the coupling in more detail, we plot in Fig. 3 $g(\mathbf{k}_F, \mathbf{q})$, given by Eqs. (16) - (18), as a function of transferred momenta \mathbf{q} along two directions as indicated. The dependency on transferred momenta arises from the nature of the charge-transfer coupling of the different modes. The c -axis modes (Figs 3a1-2,4 and 3b1-2,4), being electrostatic in nature, translate into stronger coupling for small momentum transfers, while the deformation-type coupling of the breathing branches gives stronger coupling at large \mathbf{q} , and vanishes in the limit $\mathbf{q} \rightarrow 0$ (Figs. 3a3 and 3b3).

Apart from the breathing modes, an appreciable fermionic wavevector dependence of the couplings to the c -axis modes is found as a consequence of the character of the underlying atomic vibrations. For the case of the A_{1g} and apical modes, for momentum transfers along the zone diagonal (Figs. 3b1 and 3b4, respectively), the fermionic dependence is symmetric with respect to reflections about $\pi/4$ while the B_{1g} coupling (Fig. 3b2) changes sign. Momentum transfers along the zone face (Figs. 3a1, 3a2, 3a4) do not obey any set selection rule, although the symmetric- or anti-symmetric-like character of the coupling is evident. Finally, the strong momentum dependence of the charge transfer along the c -axis dictates that the apical coupling vanishes for any fermion momentum along the zone diagonal (Fig. 3b4).

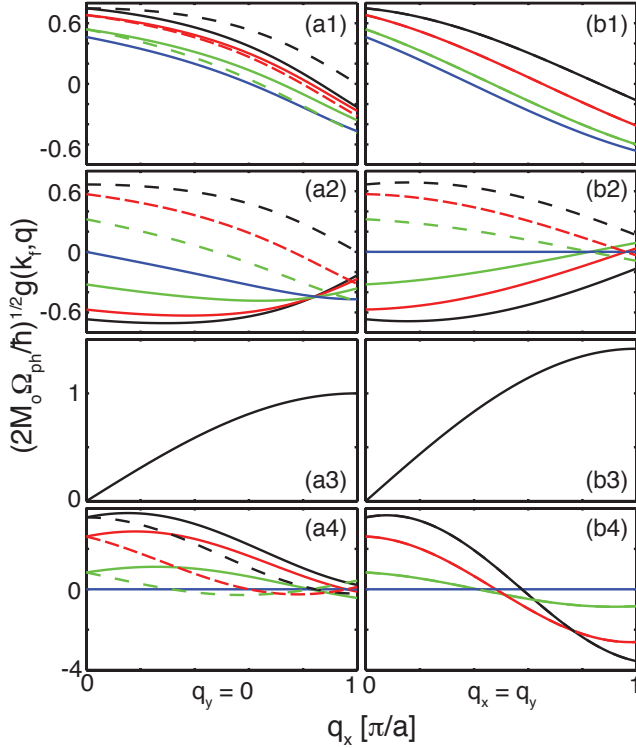


FIG. 3: (Color online) Plots of the el-ph coupling constant $g(\mathbf{k}_F, \mathbf{q})$ for fermionic momentum on the Fermi surface as a function of transferred momentum ($q_x, q_y = 0$) (a1-a4) and $q_x = q_y$ (b1-b4), respectively. a1,b1 (a2,b2) plot coupling to the A_{1g} (B_{1g}) branches, respectively, a3, b3 plot coupling to the breathing branch and a4,b4, plots coupling to the apical branch. The colors denote angles from the corner of the BZ (shown in the inset of Fig. 4) given by solid black - 0° , solid red - 15° , solid green - 30° , solid blue - 45° (nodal), dashed green - 60° , dashed red - 75° and dashed black - 90° (anti-nodal).

B. Momentum dependence on the Fermi surface

The strong dependence of $g(\mathbf{k}, \mathbf{q})$ on both \mathbf{k} and \mathbf{q} leads to anisotropic coupling between electrons and phonons. As the most relevant scattering processes involve those states near the Fermi level, the explicit momentum dependence as seen in ARPES is most clearly envisioned by calculating k -dependent self-energies, in terms of el-ph coupling λ . We take the modes to be dispersionless $\Omega_{\mathbf{q},\nu} = \Omega_\nu$, which couple to electrons via the Fock piece of the electron self-energy $\lambda_\nu(\mathbf{k})$ in lowest order⁷⁹:

$$\begin{aligned} \lambda_\nu(\mathbf{k}) &= \frac{2}{N\Omega_\nu} \sum_{\mathbf{p}} |g(\mathbf{k}, \mathbf{q})|^2 \delta(\xi_{\mathbf{p}}) \\ &= \frac{2N_F}{\Omega_\nu} \langle |g(\mathbf{k}, \mathbf{q})|^2 \rangle_{\mathbf{p}_{FS}} \end{aligned} \quad (19)$$

with $\xi_{\mathbf{p}} = \epsilon(\mathbf{p}) - \mu$, μ is the chemical potential, N is the number of momentum points and $N_F = \frac{1}{N} \sum_{\mathbf{k}} \delta(\xi_{\mathbf{k}})$ is

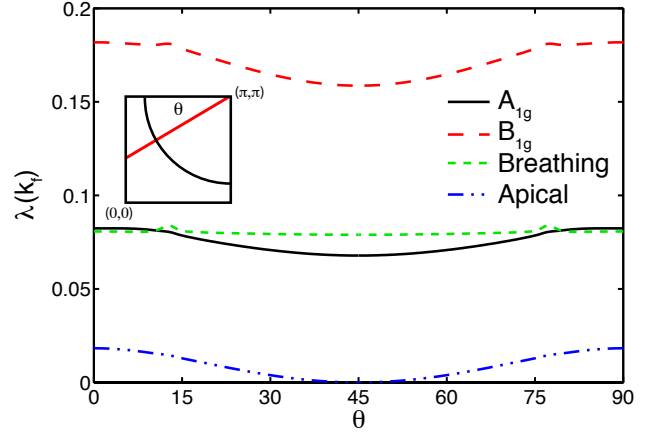


FIG. 4: (Color online) Plots of $\lambda_\nu(\mathbf{k}_F)$ for momentum points along the Fermi surface. Inset: the definition of the angle θ used in Figs. 3 and 4. The parameters used are defined in the text.

the density of states at the Fermi level. The delta function restricts the sum to initial and final fermion states \mathbf{k} , \mathbf{p} , that lie on the Fermi surface, with scattering between them governed by the transferred phonon momentum \mathbf{q} . The resulting $\lambda_\nu(\mathbf{k}_F)$ for the four modes are shown in Fig. 4. The Fermi surface contour and bandstructure are again determined from a five-parameter tight-binding bandstructure.⁷⁸ The el-ph coupling vertices are evaluated using Eqs. (16) - (18), along with the conventional parameter set (in eV): $t_{pd} = 1.1$, $t_{pp} = 0.5$, $t_{pz} = 0.29$, $t_{sp} = 2$, $t_{sz} = 1.5$, $\epsilon_{d-p} = 0.8$, $\epsilon_{d-z} = 1.00$, $\epsilon_{d-s} = -7$.^{15,80} For these parameters we obtain $A_O^2 = 0.446$, $A_{Cu}^2 = 0.592$ and $A_a^2 = 4.52 \times 10^{-2}$. Additionally, estimates of the local field strength at the planar and apical oxygen sites for Bi-2212 are used: $E_z^{plane} = 3.56$, $E_z^{apex} = 16.33$ eV/Å, respectively. A systematic derivations of these E field values across the cuprate families is given in Section V.

A strongly varying $\lambda(\mathbf{k})$ is obtained for the c -axis modes, largely weighting anti-nodal fermion states, arising from both the fermion dependence of the bare couplings as well as the small momentum transfers connecting anti-nodal points on the Fermi surface, as noted in prior treatments⁶¹ as well as more recent LDA- projected studies.⁶⁴ The anisotropy is particularly strong for the apical coupling because of the strong fermionic momentum dependence of $g(\mathbf{k}, \mathbf{q})$. On the other hand, coupling to the breathing modes has a much weaker anisotropy along the Fermi surface, due to large momentum transfers (π, π) connecting anti-nodal portions of the Fermi surface, as well as $(\pi, 0)$ and $(0, \pi)$ transfers connecting nodal points. Inclusion of a variation of the copper character across the Fermi surface yields a more anisotropic coupling.⁶¹ However, the character of the anisotropy is not as strong as that observed in Ref. 64, where the breathing branches couple more strongly to anti-nodal

Branch	λ_z	λ_ϕ
A_{1g}	7.74×10^{-2}	4.42×10^{-2}
B_{1g}	0.17	0.12
Breathing	8.27×10^{-2}	-4.75×10^{-2}
Apical	1.11×10^{-2}	0
Total	0.341	0.1149

TABLE I: Tabulated values of $\lambda_{z,\phi}$ for the four phonon branches considered in this work.

states.

The full coupling λ_z , renormalizing the single particle self-energy, is given by a sum over all modes averaged over the Fermi surface, $\lambda_z = \sum_\nu \langle \lambda_\nu(\mathbf{k}) \rangle$, and can be visualized most easily as an average over the curves shown in Fig. 4. The renormalization λ_ϕ for a $d_{x^2-y^2}$ -wave superconductor gives the el-ph contribution to the anomalous self-energy and is given by a d -wave projected average

$$\lambda_\phi = 2 \sum_\nu \frac{\sum_{\mathbf{k}, \mathbf{p}} d_{\mathbf{k}} d_{\mathbf{p}} |g_\nu(\mathbf{k}, \mathbf{q})|^2 \delta(\xi_{\mathbf{k}}) \delta(\xi_{\mathbf{p}})}{N \omega_\nu \sum_{\mathbf{k}} d_{\mathbf{k}}^2 \delta(\xi_{\mathbf{k}})} \quad (20)$$

where $\mathbf{q} = \mathbf{p} - \mathbf{k}$ and d -wave basis function $d_{\mathbf{k}} = [\cos(k_x a/2) - \cos(k_y a/2)]/2$, as before. A positive (negative) λ_ϕ denotes an attractive (repulsive) pair interaction in the $d_{x^2-y^2}$ channel. The λ values obtained for the four phonon branches considered in this work are given in table I. As noted before, the A_{1g} and B_{1g} modes enhance d -wave pairing, the breathing modes suppress it and the apex modes give no contribution. We note that these values for the λ_z are similar to those obtained from recent LDA results for $\text{YBa}_2\text{Cu}_3\text{O}_7$ ^{64,65} but are smaller than those calculated for doped CaCuO_2 .^{23,24} We again remark that important consequences of screening are not considered here, which can affect both the magnitudes and anisotropies of the couplings as will be discussed in Sec. IV.

C. Kinematic constraints

It is important to note that in ARPES there is a strong kinematic constraint that also governs which fermion states can couple to each mode. Due to energy conservation of scattering from dispersionless phonons, the normal state ARPES spectra may show mixing of electron and phonon states if the band energy along a particular cut crosses the phonon mode energy. This gives rise to a kink in the dispersion, with trailing intensity observed asymptotically to the phonon mode energy. Otherwise, if the band along a particular cut lies above the mode energy, the spectra may show level repulsion in the form of a flattened band bottom along that cut.

In the cuprates, the shallow band near the anti-nodal parts of the BZ limits the couplings of those states to only modes with energies less than $\xi(0, \pi)$. Thus, quite

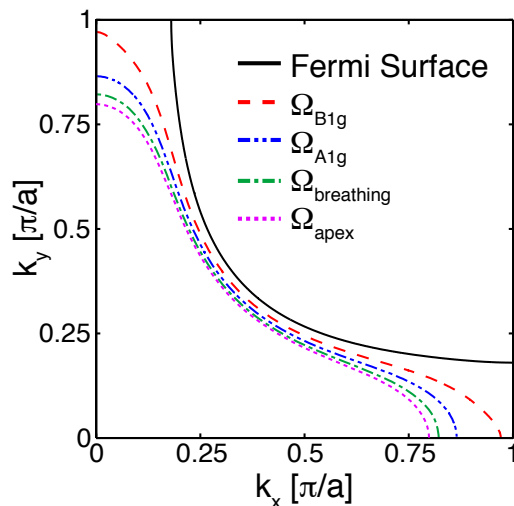


FIG. 5: (Color online) A contour plot of the band structure of optimal doped Bi-2212 obtained from the five-parameter tightbinding model of Ref. 78. The outermost contour (solid black) corresponds to the FS. The remaining contours correspond to $\epsilon_{\mathbf{k}} - \mu = \Omega_\nu$ for the four phonon branches considered in this work. Reading from the FS to the Γ -point, the contours correspond to the B_{1g} , A_{1g} , breathing and apical branches, respectively.

generally, we would expect coupling to the modes to disappear from the spectra when $\Omega_\nu < \xi(\mathbf{k})$ along the entire cut. The contours $\xi(\mathbf{k}) = \Omega_\nu$, which define this kinematic constraint, are plotted in Fig. 5 at optimal doping. The Fermi level is also shown for reference and corresponds to the outermost contour (solid black). In the case of the apical mode, although the coupling may be largest for \mathbf{k}_{AN} , a kink effect is prevented kinematically. Moreover, the breathing modes will be observable only for near-nodal cuts due to the form of the coupling as well as the energies of the modes which are large when compared to the A_{1g}/B_{1g} modes and the saddle point energy $\xi(0, \pi)$. In fact, for optimally doped Bi-2212, the B_{1g} modes lie right at $\xi(0, \pi)$, and can be seen most clearly in the anti-nodal directions, although its coupling should be felt across the entire Fermi surface as shown in Fig. 4.

In the superconducting state, the energy contours shift by the maximum value of the energy gap and are set by $\Omega_\nu + \Delta_0$, and the kinematic range shrinks for coupling to the higher energy modes.^{61,81}

IV. POOR SCREENING ALONG THE c -AXIS

A. Overall Approach

Screening - responsible for reducing the net el-ph coupling in conventional good metals - must be included for all c -axis phonons. In the usual treatment of screening,⁸²

the screened el-ph coupling \bar{g} is

$$\bar{g}(\mathbf{k}, \mathbf{q}, \Omega) = g(\mathbf{k}, \mathbf{q}) + \frac{V(q)\Pi_{g,1}(q, \Omega)}{1 - V(q)\Pi_{1,1}(q, \Omega)} \quad (21)$$

where $V(q) = 4\pi e^2/q^2$ is the 3D Coulomb interaction and $\Pi_{a,b}(q, \Omega)$ is the frequency-dependent polarizability calculated with vertices a, b , respectively. Since the plasmon frequency Ω_{pl} is usually much larger than the phonon frequencies in 3D metals, in the limit $\mathbf{q} \rightarrow 0$ the effective coupling is $\bar{g}(\mathbf{k}, \mathbf{q} \rightarrow 0) - \delta g$ with δg denoting the average value of $g(\mathbf{k}, \mathbf{q})$ over the Fermi surface. Thus the bare el-ph coupling is normally well screened.

Turning now to the cuprates, from the point of view of Coulomb interactions, the materials are 3D with $q^2 = q_{2D}^2 + q_z^2$ and $\mathbf{q}_{2D} = (q_x, q_y)$. However, due to the largely incoherent c -axis transport observed across the phase diagram (apart from the overdoped side), the polarizability is largely determined by the planar conduction electrons and $\Pi_{a,b}(q, \Omega) = \Pi_{a,b}^{2D}(q_{2D}, \Omega)$. As a result, important changes to the effects of screening occur for small $\mathbf{q}_{2D} \ll \mathbf{q}$.

A qualitative feel for the effects of poor screening can be obtained by considering a coupling which is independent of Fermion momentum \mathbf{k} and in the limit of small in-plane momentum transfers, where $v_F q_{2D} \ll \Omega_{ph}$. This limit is most relevant for Raman active phonons and $\Pi_{1,1}(q, \Omega_{ph}) = nq_{2D}^2/m\Omega_{ph}^2$, with $n/m = 2/V_{cell} \sum_{\mathbf{k}} f(\epsilon_{\mathbf{k}}) \frac{\partial^2 \epsilon_{\mathbf{k}}}{\partial k_x^2}$ and $\Pi_{g,1}(q, \Omega_{ph}) = \frac{nq_{2D}^2}{m_g(q)\Omega_{ph}^2}$, with $n/m_g(q) = 2/V_{cell} \sum_{\mathbf{k}} f(\epsilon_{\mathbf{k}}) g(\mathbf{q}) \frac{\partial^2 \epsilon_{\mathbf{k}}}{\partial k_x^2}$ where V_{cell} is the unit cell volume and f is the Fermi distribution. The screened el-ph interaction is then

$$\bar{g}(\mathbf{k}, \mathbf{q}, \Omega_{ph}) = g(\mathbf{q}) - \frac{m}{m_g(q)} \frac{\Omega_{pl}^2(q)}{\Omega_{pl}^2(q) - \Omega_{ph}^2}, \quad (22)$$

with $\Omega_{pl}^2(q) = \Omega_{pl}^2 \cdot (q_{2D}/q)^2$. Thus c -axis Raman-active phonons in the cuprates, with couplings strongest for small momentum transfers \mathbf{q} and $\Omega_{pl}(q) < \Omega_{ph}$, should survive the effects of screening.

B. Considerations for the polarizability and λ_ν

To evaluate the polarizabilities in the cuprates, we use the standard Lindhard expression

$$\begin{aligned} \Pi_{a,b}(q, \Omega) &= \frac{2}{V_{cell}} \sum_{\mathbf{k}} a(\mathbf{k}, \mathbf{q}) b(\mathbf{k}, \mathbf{q}) \\ &\times \frac{f(\epsilon_{\mathbf{k}}) - f(\epsilon_{\mathbf{k}+\mathbf{q}})}{\epsilon_{\mathbf{k}} - \epsilon_{\mathbf{k}+\mathbf{q}} + \Omega + i\delta}, \end{aligned} \quad (23)$$

with all wavevectors being two-dimensional. This form of the polarizability has been considered in previous works focusing on the role of screening and reduced dimensionality in the doping-dependent softening of the in-plane bond-stretching modes.^{83,84} For the Coulomb interaction

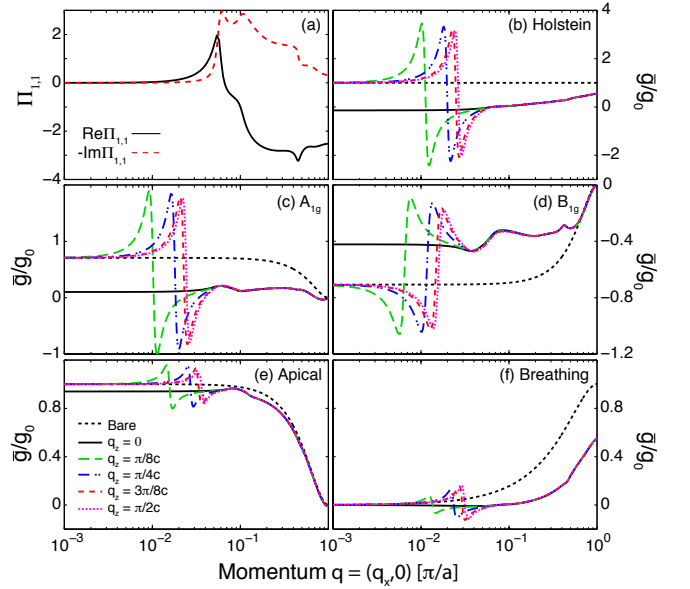


FIG. 6: (Color online) (a) Plots of the real (black) and imaginary ($-1 \times$, red) parts of the charge susceptibility $\Pi_{1,1}$ and (b)-(f) the renormalized el-ph coupling $\bar{g}(\mathbf{k}, \mathbf{q})$ in arb. units for $\mathbf{k} = (0, \pi/a)$ and $\mathbf{q} = (q_x, 0)$ for different values of q_z as indicated by the legend. For (b)-(f) the black dashed line corresponds to the bare coupling $g(\mathbf{k}, \mathbf{q})$. A momentum-independent bare coupling is considered in (b), followed by the A_{1g} , B_{1g} , apical and breathing modes in (c)-(f), respectively. In the case of the breathing modes a small q_y component has been added to visualize the effects of screening at small \mathbf{q}_{2D} . The q_x axis in all plots is on a logarithmic scale to highlight the small \mathbf{q}_{2D} region.

$V(q)$, more appropriately for the cuprates, we consider a layered system with charge density essentially confined to 2D layers, Coulombically coupled across the planes:^{85,86}

$$V(q_{ab}, q_z) = \frac{V}{q_{ab} a \tanh(q_{ab}/q_0)} \frac{1}{1 + F_z^2} \quad (24)$$

where $V = 2\pi e^2/a\sqrt{\epsilon_{ab}\epsilon_c}$, $q_0 = (4/c)\sqrt{\epsilon_c/\epsilon_{ab}}$ with $\epsilon_{ab,c}$ the in-plane, out-of-plane dielectric constants, respectively. The c -axis lattice constant sets the in-plane momentum scale beyond which the planes become effectively uncoupled, and leads to an interpolation between the 2D and 3D form for the Coulomb interaction where $F_z = \sin(q_z c/4)/\sinh(q_{ab}/q_0)$ provides the q_z dispersion of the interaction.

The real and imaginary parts of the pure charge polarizability $\Pi_{1,1}$ are plotted in Fig. 6a. Here, $\delta = 5$ meV has been included to smooth singularities, $\epsilon(\mathbf{k})$ is taken for optimal doping in Bi-2212,⁷⁸ $c = 30.52$ Å, $a = 3.8$ Å, and in-plane⁸⁷ and out-of-plane⁸⁸ conductivities yield $\epsilon_{ab} \sim \epsilon_c = 4.8$ for the high-frequency dielectric constants, which determine the plasma frequency. For this choice in parameters we obtain $\Omega_{pl} = 0.914$ eV at optimal doping in agreement with Ref. 87. In order to calculate the screened el-ph vertex the static dielectric constants

must be used in Eq. (24). Here, we take $\epsilon_c(0) = 10$, which is obtained from optical measurements,⁸⁸ and set $\epsilon_{ab}(0) = 4\epsilon_c(0)$. This choice in ratio results in a factor two reduction in the breathing vertex at $\mathbf{q} = (0, \pi)$ which is consistent with Ref. 32. Additionally, we have set $\Omega = 60$ meV in Fig. 6a. The real part of $\Pi_{1,1}$ rises as q^2 before abruptly falling as the imaginary part rises when the condition $v_F q = \Omega$ is satisfied. These kinematic constraints give similar forms for the mixed polarizabilities $\Pi_{g,1}$, although the detailed q dependence may be slightly different.

In Fig. 6b-f several renormalized (screened) el-ph vertices $\bar{g}(\mathbf{k}_{AN}, q_x, \Omega_{pl})$ are plotted for each of the modes considered in this work. Here $\mathbf{k}_{AN} = (\pi, 0)$ and the momentum transfer is taken along the zone face $\mathbf{q} = (q_x, 0)$ and \bar{g} is plotted for several values of q_z as indicated. To illustrate the effects of poor screening of the long-range Coulomb interaction, in Fig. 6b, a momentum-independent bare coupling $g = 1$ (arb. units) is also shown. For a momentum-independent vertex $\Pi_{g,1} = g\Pi_{1,1}$. In this case, for $\Omega \ll \Omega_{pl}(q)$ and $q_z = 0$ screening is perfect, leaving only a small el-ph interaction at large \mathbf{q}_{2D} . This can be seen as the black line, which corresponds to $q_z = 0$ in Figs. 6b-f. For finite q_z a small cone of wavevectors satisfies $\Omega \geq \Omega_{pl}(\mathbf{q})$ where screening is inoperable and the renormalized vertex recovers the bare value. This enhancement of the small q coupling occurs over a small range of q -vectors until (\mathbf{q}_{2D}, q_z) satisfy $\Omega_{pl}(q) = \Omega_{ph}$, where a logarithmic divergence occurs which is cut-off by damping. For increasing q_z this condition moves to a progressively larger \mathbf{q}_{2D} and a window of momentum points opens where the vertex can be well-represented by its bare value.

Likewise, Fig. 6c-f plot the renormalized couplings for the A_{1g} , B_{1g} , apical and breathing modes, respectively. For large in-plane momentum transfers \mathbf{q}_{2D} the c -axis couplings are largely unaffected by screening due to the fall-off of the polarizability at large \mathbf{q}_{2D} . However, for the breathing branch, where the bare coupling weights large momentum transfers, the growth of the mixed polarizability leads to an overall suppression of the screened vertex at large momentum transfers. For small in-plane momentum transfers - relevant for c -axis Raman active phonons considered here - screening is ineffective and the coupling is anomalously enhanced over large q coupling. Again, for the breathing branch, only small effects are noticed at small \mathbf{q}_{2D} due to the nature of the deformation-type coupling for these modes. Since we have neglected any fermionic dependence on the bare breathing couplings, the mixed polarizability is equal to the pure charge polarizability in this case.

Using Eq. (22) the momentum-dependent el-ph coupling strength $\lambda_\nu(\mathbf{q}_{2D})$

$$\lambda_\nu(\mathbf{q}_{2D}) = \frac{2N_F}{N_c\Omega_\nu} \sum_{\mathbf{k}, q_z} \langle |\bar{g}_\nu(\mathbf{k}, \mathbf{q}, \Omega_{pl})|^2 \rangle \quad (25)$$

is plotted in Fig. 7 as a function of \mathbf{q}_{2D} (on a log scale to highlight the small \mathbf{q} behavior) for $\nu = A_{1g}$, B_{1g} , apical

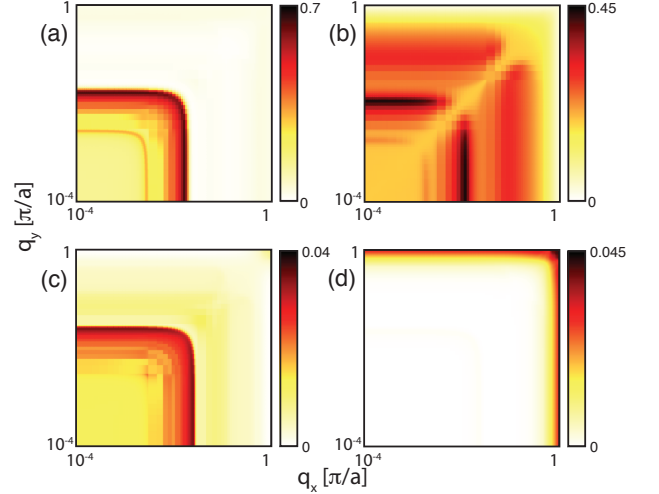


FIG. 7: (Color online) Plots of the momentum dependent coupling $\lambda_\nu(\mathbf{q}_{2D})$, Eq. (25), for $\nu = A_{1g}$ (a), B_{1g} (b), apical (c) and bond-stretching (d) modes. The coupling are plotted on a logarithmic scale for \mathbf{q}_{2D} to highlight the region of poor screening.

and bond-stretching modes shown in panels Fig. 7(a)-(d), respectively. One can clearly see that when summed over all out-of-plane momentum transfers q_z , the net coupling is on the order of the bare coupling for small \mathbf{q}_{2D} , while the coupling at large \mathbf{q} is suppressed. The fermionic momentum dependence of the bare vertices for the B_{1g} case noticeably alters $\lambda(\mathbf{q}_{2D})$ for momentum transfers along the BZ diagonal where it is largely projected out. The A_{1g} and apical $\lambda(\mathbf{q}_{2D})$ are quite similar even though the anisotropy of the bare interaction is substantially different and weights different regions of the BZ. For all the c -axis modes, coupling is small for $\mathbf{q}_{2D} = \mathbf{Q}_{AF} = (\pi/a, \pi/a)$. Since we have neglected Hubbard short-range Coulomb repulsion, which further suppresses coupling at large momentum transfers,³⁵ Raman c -axis modes are thus not expected to appear in transport measurements. Likewise, the breathing modes are altered at small \mathbf{q}_{2D} , but the overall coupling does not give much weight for these transfers. Since the apical and B_{1g} modes strongly favor coupling to the anti-nodal fermions, we may conclude that the underlying density of states, combined with the fermionic momentum dependence, strongly influences the magnitude of the couplings at small \mathbf{q}_{2D} ; the phonon and eigenvectors control the actual angular dependence while the nature of the coupling - electrostatic or deformation - controls the $|\mathbf{q}|$ -dependence.

This \mathbf{q} -dependence strongly affects the d -wave projected pair interaction as well. In Fig. 8 we plot the d -wave projected coupling

$$\lambda_{\nu,d}(\mathbf{q}_{2D}) = \frac{2N^d}{N_c\Omega_\nu} \sum_{q_z} \langle |\bar{g}(\mathbf{k}, \mathbf{q}, \Omega_{pl})|^2 d_{\mathbf{k}} d_{\mathbf{k}-\mathbf{q}} \rangle_{\mathbf{k}_{FS}}^d \quad (26)$$

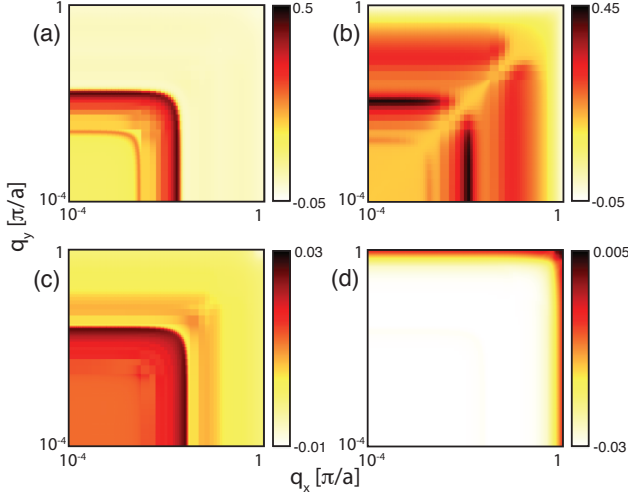


FIG. 8: (Color online) Plots of the d -wave coupling $\lambda_{\nu,d}(\mathbf{q}_{2D})$, Eq. (26), for $\nu = A_{1g}$ (a), B_{1g} (b), apical (c) and bond-stretching (d) modes. The coupling is plotted on a logarithmic scale for \mathbf{q}_{2D} to highlight the region of poor screening.

for the same modes considered in Fig. 7. As with Fig. 7, $\lambda_{\nu,d}(\mathbf{q}_{2D})$ has been plotted on a log scale in order to highlight behavior at small \mathbf{q}_{2D} . One can see straightforwardly that the phonons that strongly favor small \mathbf{q} scattering largely promote d -wave pairing (the c -axis modes) while phonons that favor large \mathbf{q} -scattering, such as the bond-stretching modes, are detrimental. Furthermore, for the bond-stretching modes, while a large region of q space supports pairing, the large weight near $\mathbf{q} = \mathbf{Q}$ dominates the coupling. The consequence of poor screening for finite q_z transfers, which accentuates small q couplings, is to enhance the overall d -wave coupling compared to $q_z = 0$ as well as standard Debye screening ($\Omega_{pl} \gg \Omega_{\nu}$) for c -axis modes, and diminishes the repulsive part for the bond-stretching modes.

To visualize the effect of screening on the fermionic dependence of the coupling, we plot in Fig. 9 the screened $\lambda_{\nu}(\mathbf{k}_{FS})$, derived from Eq. (19) where g has been replaced with \bar{g} from Eq. (22). Here, to mimic the effect of doping in the cuprates, we have varied the plasma frequency to smaller values in accordance with experiment, reflecting the increased insulating behavior and ionicity along the c -axis that occurs with underdoping in the phase diagram of hole-doped cuprates. The values for the total coupling $\lambda_z = \sum_{\nu} \langle \lambda_{\nu}(\mathbf{k}) \rangle$ and λ_{ϕ} defined in Eq. (20) are shown in Fig. 10.

Screening causes several noticeable effects compared to the unscreened case shown in Fig. 4. In order to mimic the effects of doping the screened el-ph vertex for the four branches is shown for Ω_{pl} ranging from 290 to 914 meV. (The black arrows indicate the direction of increasing Ω_{pl} .) As the plasma frequency is increased the A_{1g} , apical and breathing branches can be screened more effectively and the overall vertex is lowered around the Fermi

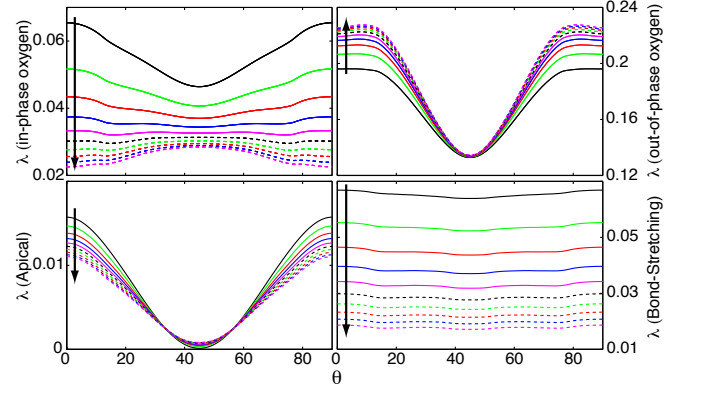


FIG. 9: (Color online) Plots of the screened e-ph $\lambda(\mathbf{k}_F)$ for fermions at the Fermi level as a function of θ for several values of the plasma frequency Ω_{pl} . The value of Ω_{pl} varies from 0.289 eV (black, solid) to 0.914 eV (purple, dashed). The black arrows indicate the direction of increasing Ω_{pl} . The parameters used to generate this figure are defined in the text.

surface. In the case of the A_{1g} and apical c -axis branches, the largest effect occurs in the anti-nodal region where the bare vertex is largest. In the case of the B_{1g} branch there is an anomalous anti-screening which occurs and the B_{1g} vertex in the antinodal region is enhanced with increasing Ω_{pl} . This non-intuitive result is due to the out-of-phase oscillations of the oxygen modes since the only difference between the bare vertices for the A_{1g} and B_{1g} branches is the phase of the phonon eigenvectors. From these results it is evident that the self-energy due to coupling to c -axis phonons should redistribute weight around the Fermi surface as the number of doped holes varies. Thus, we infer that in the cuprates a window in q -space at small \mathbf{q}_{2D} occurs in which the el-ph interaction can still be quite large and avoid screening. This would not occur if the material was fully conducting along the c -axis and this effect increases with underdoping as Ω_{pl} is reduced with decreasing hole concentration.

In contrast, since poor screening does not affect large momentum transfers, the strength of the breathing coupling dramatically increases for smaller Ω_{pl} . This implies that the electron self-energy contribution from the breathing branches should grow with underdoping. Once again, however, we remark that this finding must be viewed with caution since large \mathbf{q} -behavior is governed strongly by Coulomb interactions.

Finally, in Fig. 10 we plot the total coupling $\lambda_{z,\phi}$ resulting from the screened el-ph vertex as a function of Ω_{pl} . Following the trends in Fig. 9, the total coupling in both channels decreases with increasing Ω_{pl} for the in-plane breathing branch, as well as the apical and A_{1g} branches, while the coupling to the B_{1g} branch is enhanced. In the case of the d -wave coupling, the attractive interaction of the A_{1g} branch is largely cancelled by the repulsive interaction of the breathing branch. Therefore, the total attractive interaction for d -wave pairing, which is primarily provided by the B_{1g} branch, is expected to

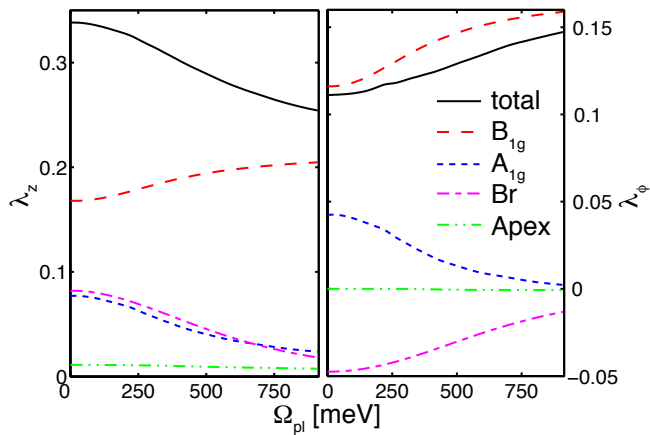


FIG. 10: (Color online) Plots of λ_z (left) and λ_ϕ (right) as a function of the plasma frequency Ω_{pl} . The parameters taken are defined in the text.

be enhanced with progressive overdoping.

The transition from insulating to more metallic behavior, reflected in Ω_{pl} , is one aspect of the doping dependence expected for el-ph coupling. However, this is not the only change expected to occur with doping. As a sample is doped away from half-filling the character of the $pd-\sigma^*$ band is expected to change as spectral weight redistributes itself within the quasiparticle and lower and upper Hubbard bands.⁸⁹ This will be reflected in the parameters A_O , A_a and A_{Cu} . Since these parameters enter the el-ph vertices in the fourth power, doping-induced changes in the bandstructure can have a large impact on the strength of the el-ph coupling. The value of the local crystal fields are also expected to vary with doping. This was shown in Ref. 90, which examined the role of an interstitial oxygen dopant in the SrO/BiO layers of Bi-2212 and found that the dopant locally enhanced E_z at the planar oxygen site by up to a factor of five. The structural details of the crystal can also induce changes to the character of the band at Fermi level (A_O , A_{Cu} and A_a), through variations in the Madelung energies of the atoms and the degree of hybridization between the CuO_2 plane and off-plane atoms such as the apical oxygen. Due to these considerations the overall strength of the el-ph coupling can have a complex dependence on both the carrier concentration of the CuO_2 plane as well as the composition and structure of the material. In the next section we examine the materials dependence of the el-ph interaction by conducting a systematic examination of the role of structure in determining the strength of the interaction across various families of high- T_c cuprates.

V. MADELUNG ENERGIES AND LOCAL FIELDS

The environment around the CuO_2 plane influences electron dynamics in the plane via the Madelung ener-

gies and local crystal fields. As a result, local symmetry breaking plays an important role in lattice dynamics. For example, X-ray measurements on $\text{YBa}_2\text{Cu}_3\text{O}_7$ ⁹¹ have shown that the CuO_2 planes are statically buckled, and a linear el-ph coupling results from the breaking of local mirror plane symmetry. LDA calculations for the infinite layer material CaCuO_2 also found evidence for static buckling of the plane due to the steric interactions among the oxygen $2p_z$ orbitals which produces a substantial linear B_{1g} el-ph coupling.²⁴ Among the different contributions to local symmetry breaking, this section is devoted to an investigation of the magnitude of the Madelung energies and local fields across families of the cuprates as a mechanism of local symmetry breaking.

We remark that LDA investigations of el-ph coupling are limited mostly to stoichiometric YBCO, with virtual crystal extensions to LSCO and CaCuO . LDA bandstructure, being metallic in nature, will tend to screen charge variations whereas those charge variations, particularly off the CuO_2 plane, may be unscreened and result in strong local modifications of band parameters triggering nano-scale inhomogeneity as well as strong variations of el-ph coupling. This was demonstrated in Ref. 90, where it was shown that the presence of an interstitial oxygen dopant's unscreened charge in the SrO/BiO layers produced large local enhancements in the crystal field strength at the planar oxygen sites. This resulted in a local increase in the strength of the coupling to the A_{1g} and B_{1g} branches, which in turn reduced the energy gap and broadened the spectral features in the hole addition/removal spectrum as well as locally increased J via the gain in lattice energy.

Here, we focus our calculations in the ionic limit, where the ions are represented as point charges, and evaluate the electrostatic sums using Ewald's method. We show that the Madelung potential landscape is sensitive to the details of the unit cell, producing material-dependent variations in the field strength at the planar and apical oxygen sites. For the field at the oxygen site of the outermost CuO_2 plane, which determines the coupling to the A_{1g} and B_{1g} modes, this variation mirrors the observed variations in T_c suggesting a link between these quantities. The use of formal valences in the electrostatic calculations reflects the stoichiometric compounds and therefore the estimates obtained from their use corresponds to the parent compounds. However, in light of the findings of Ref. 90, we also address doping-induced changes in the crystal field strength in Bi-2212 in order to assess how these fields are expected to vary with doping. Finally, the variations in $\lambda_{z,\phi}$ that arise as a function of material due to the electrostatic considerations presented here are also discussed. Here we focus on the B_{1g} mode, which has the largest contribution to d -wave pairing and take into account variations in the local field, relative shifts in site energies, and changes in the atomic character of the band, all of which are directly affected by the details of the crystal structure.

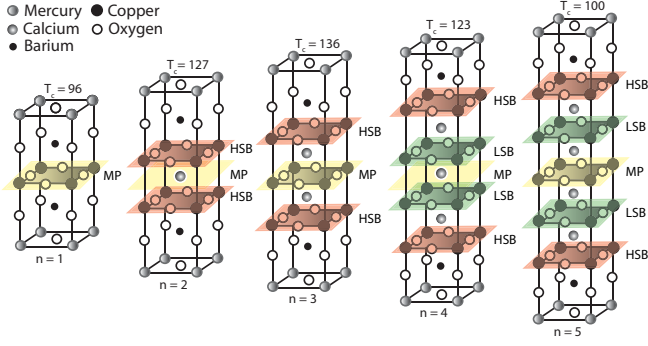


FIG. 11: (Color online) The $\text{HgBa}_2\text{Ca}_{n-1}\text{Cu}_n\text{O}_{4n+\delta}$ ($n = 1 - 5$) unit cell showing the locations of the mirror plane (yellow, MP), low symmetry breaking plane (green, LSB) and high symmetry breaking planes (red, HSB). The degree of symmetry breaking establishes the strength of the electric field which couples to the c -axis phonons.

A. Formal Valences: The Parent Compounds

A structural view of the lattice across the Hg family, as shown in Fig. 11. Starting with $n = 1$ shows that the coupling to planar oxygen c -axis phonons must be weak, while couplings involving the apical oxygen phonon can be strong due to the asymmetry along the c -axis at the apical site (CuO_2 on one side and HgO on the other). For $n > 1$ the outer layer does not lie in a mirror-plane and the coupling strength depends on the local asymmetry (in this case BaO on one side, Ca on the other). However, the innermost plane may lie in a mirror plane when n is odd, while the intermediate planes will generally have a weaker degree of symmetry breaking in comparison to the outermost plane. Thus, in the context of el-ph coupling, the most strongly coupled modes will be those involving displacements of the apical and planar oxygen atoms in the outermost layers. In Hg compounds the local asymmetry around the outermost plane is due to Ca and BaO structures on opposite sides of the CuO_2 plane. In YBCO it is due to Ca and SrO structures. Such changes in composition will affect the magnitude of the crystal field and these differences can be quantified by examining the Madelung potential for the apical and planar oxygen sites for the Hg, Tl and Bi cuprate families.

The electric field strength can be regarded as the first derivative of the Madelung potential, which consists of a contribution of all electrostatic interactions between ions in the solid. For a test charge q_t , located at position \mathbf{r} , the Madelung potential Φ is defined as:

$$\Phi = q_t \int d\mathbf{r}' \frac{\rho(\mathbf{r}')}{|\mathbf{r} - \mathbf{r}'|} \quad (27)$$

where ρ is the charge density. In the ionic limit the charge density is comprised of point charges $\rho(\mathbf{r}) = \sum_i \delta(\mathbf{r} - \mathbf{R}_i)$, where the sum i is taken over the atoms of the crystal located at \mathbf{R}_i .

There are several common methods used to calculate

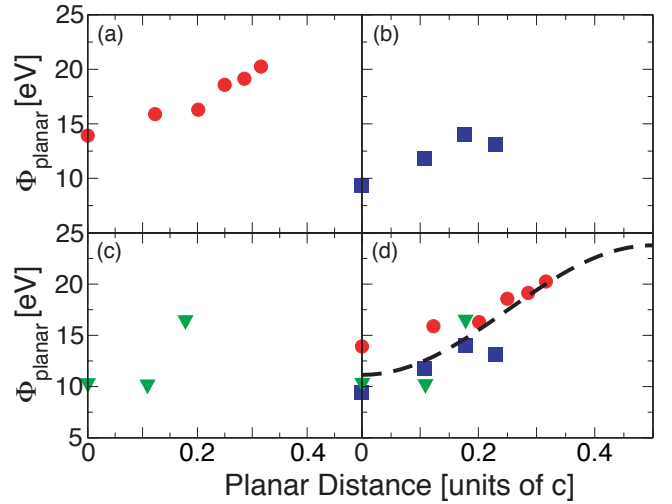


FIG. 12: (Color online) The Madelung potential at the CuO_2 planar oxygen site as function of distance from the plane of mirror symmetry: (a) $\text{HgBa}_2\text{Ca}_{n-1}\text{Cu}_n\text{O}_{2n+2}$ ($n = 1-6$, red circles). (b) $\text{Tl}_2\text{Ba}_2\text{Ca}_{n-1}\text{Cu}_n\text{O}_{2n+2}$, ($n = 1-4$, blue squares). (c) $\text{Bi}_2\text{Sr}_2\text{Ca}_{n-1}\text{Cu}_n\text{O}_{2n+2}$ ($n = 1-3$, green triangles). (d) An overlay of the Hg, Tl and Bi plots rescaled by the lattice spacing, a . The black line is a fitted curve of the form $a\Phi = A + B \cos(2\pi z/c)$.

the Madelung potential. A general and powerful method was given by Ewald,^{92,93} which is used here to determine the Madelung energies for the planar and apical oxygen sites in the outermost CuO_2 planes in the unit cell for Bi ($n=1-3$), Tl ($n=1-4$) and Hg ($n=1-6$) cuprates. The atomic positions are obtained from the known structural data given in Refs. 94–107. In all cases formal valence charges for the ions have been assumed. It should be noted that for the materials considered herein, the surfaces are non-polar, as opposed to $\text{YBa}_2\text{Cu}_3\text{O}_7$ (YBCO).⁹³ Therefore the surface termination layer is not critical for our calculations.

In the case of YBCO, assuming that the surface is terminated between the BaO and CuO sublayers, a local field between 0.8 - 2.1 eV/Å was obtained, arising from the asymmetry condition of Y^{3+} and Ba^{2+} on either side of the CuO_2 plane.⁹³ This polar surface contribution overwhelms the periodic contribution from Ewald's method. Without the polar contribution, the coupling for example to the B_{1g} mode is underestimated when compared to that obtained from periodic LDA methods. In Ref. 93 it was shown how deviations away from formal valences can give much different values for the local crystal fields. We have also found that the local electric fields are more sensitive than the Madelung energy to small structural distortions and deviations away from formal valences. Therefore we conclude that while the overall field values should be viewed as being approximate, we assume that the variations across the different materials can be qualitatively compared.

The Madelung energies of the planar and apical oxy-

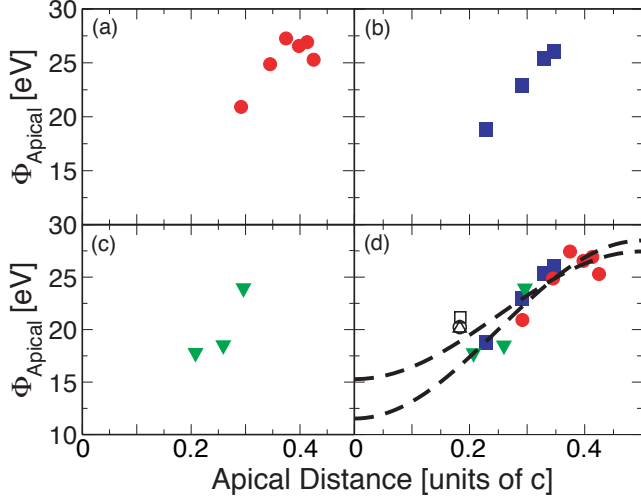


FIG. 13: (Color online) The Madelung energy of the apical oxygen site as a function of distance from the plane of mirror symmetry: (a) $\text{HgBa}_2\text{Ca}_{n-1}\text{Cu}_n\text{O}_{2n+2}$ ($n = 1-6$, red circles). (b) $\text{Tl}_2\text{Ba}_2\text{Ca}_{n-1}\text{Cu}_n\text{O}_{2n+2}$, ($n = 1-4$, blue squares). (c) $\text{Bi}_2\text{Sr}_2\text{Ca}_{n-1}\text{Cu}_n\text{O}_{2n+2}$ ($n = 1-3$, green triangles). (d) An overlay of the Hg, Tl and Bi plots in addition of points obtained for LSCO and LBCO (black open symbols). The dashed and solid black lines are fitted curves of the form $a\Phi = A + B \cos(2\pi z/c)$. The dashed curve is obtained when all of the data is included while the solid curve is obtained when the La data points are excluded.

gen sites are plotted in Figs. 12 and 13, respectively, and plotted as a function of the distance between outermost CuO_2 plane (or apical oxygen) and the mirror plane located at the center of the unit cell. The calculated apical Madelung energies are in agreement with those obtained in Ref. 15 for similar structural data, while the Madelung energies for the planar sites are, to the best of our knowledge, presented here for the first time. One can see that the Madelung energies for both the planar and apical sites increase when the outermost CuO_2 plane lies further from the center of the unit cell. This occurs both when the number of planes per unit cell is increased as well as when the layers are spaced closer to the charge reservoir due to the larger spacer ions between the CuO_2 layers. Scaling the Madelung energies by the in-plane lattice constant a collapses the data for each cuprate family onto a single curve, as shown in subpanel (d) of Figs. 12 and 13. By symmetry, the electric field falls to zero at a mirror plane implying that $\Phi(z/c)$ must have zero slope at these points. If z is measured relative to the mirror plane, such as those indicated in Fig. 11, then the simplest function that satisfies these boundary conditions is $a\Phi(z/c) = A + B \cos(2\pi z/c)$, and serves as an overall guide for describing the behavior of the data. For the planar oxygen sites we obtain $A = 66.3$, $B = -24.0$ while for the apical oxygen sites $A = 81.2$, $B = -23.1$ ($A = 76.0$, $B = -32.2$ when the points for the La family are excluded), in units of $\text{eV}\cdot\text{\AA}$.

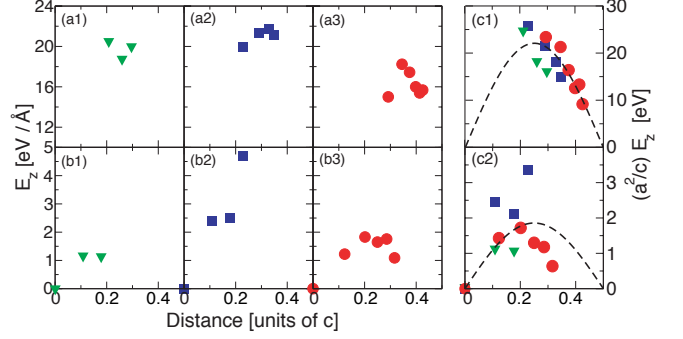


FIG. 14: (Color online) (a1)-(a3) The magnitude of the electric field at the apical oxygen site of the Hg, Tl and Bi families of cuprates, respectively. The data is plotted as a function of the apex distance from the plane of mirror symmetry located at the center of the CuO_2 planes. (b1)-(b3) The magnitude of the electric field at the planar oxygen site of the outermost CuO_2 plane for the set of same compounds. (c1)-(c3) The strength of the electric field scaled by the unit cell lattice parameters for the planar and apical oxygen fields, respectively. The dashed lines represent a fit $a^2 E(z/c)/c = A \sin(2\pi z/c)$, where $A = 7.1$ and 83.9 eV for the planar and apical sites, respectively.

Fig. 14 shows the local E fields at the apical and planar oxygen sites for the outermost CuO_2 plane in the unit cell for a number of cuprate families having different numbers of layers. For the single layer cuprates the CuO_2 plane lies in a mirror plane located at the center of the unit cell resulting in a zero field at the planar oxygen sites. Thus there is no el-ph first order coupling to the A_{1g} and B_{1g} branches in the single layer materials. This is no longer the case for $n > 1$. Examining the largest data set, that of the Hg family ($n = 1-6$), the E -field at the planar oxygen site rises from $n = 1$ and peaks for $n = 3$ where the location of the outer plane of the cell is $z/c \sim 0.2$. As n is increased beyond this point the magnitude of the crystal field begins to decrease. The data for the Bi- and Tl-families are consistent with this trend - generally the local fields rise and follow the associated Madelung energy as the outermost plane moves further from the center of the cell, and falls once the outermost plane moves closer to the edges of the unit cell where the Madelung energy profile flattens. Since the apical oxygen does not lie in a mirror plane for any cuprate, a finite field is allowed even for $n = 1$. Behaviour similar to the planar oxygen site is also seen with a peak field strength generally occurring for $n = 3$ and decreasing beyond this point.

The scatter in values is largely due to uncertainties in structural data as well as the oversimplified use of formal valences for all materials. However, the results are similar among the different cuprates if the position of the outermost plane relative to the center of the cell is considered. Figs. 14c1 and 14c2 show that the local field may be collapsed onto a sinusoidal curve as a function of c -axis distance when rescaled to account for the unit cell volume variations.

The presented E -field values are sensitive to the structural data, particularly for the planar oxygen sites where the degree of static Cu-O bond buckling is relatively uncertain. Since a static buckling further breaks mirror plane symmetry across the CuO_2 plane, small variations in the degree of buckling can have a large impact on the field values obtained while only having a minor effect on the Madelung energies. For example, neglecting buckling on the order of $0.001c$ in the $n = 2$ layer materials results in E -field variations on the order of 20-40 percent for the planar oxygen sites, while the variations in the corresponding Madelung energies vary only by a few percent. We have found that both the Madelung energies and local fields for the apical oxygen are not as sensitive to the degree of static buckling in the CuO_2 plane.

We now comment on the E -field values reported here in the context of previous works involving coupling to the c -axis modes. Due to the fact that Ba^{2+} and Sr^{2+} lie on either side of the CuO_2 plane in Bi-2212, previous expectations were that the planar field in this system would be smaller than that found in YBCO and work by one of the authors on the Raman derived B_{1g} phonon lineshape confirmed these expectations.¹⁰⁸ Since the T_c 's of these two materials are roughly equivalent, it was concluded that the el-ph coupling was irrelevant to the pairing mechanism. However, a re-examination of the data set, in view of the greater sample inhomogeneity and impurity effects in Bi-2212 compared to YBCO, indicates empirically that the field may not be as small as previously considered. Using the theory of Ref. 62, the Fano line-shape of the B_{1g} phonon in optimally doped Bi-2212¹⁰⁸ can be fit equivalently with a value of the coupling, parameterized by λ , which is an order of magnitude different if one assumes a large, intrinsic broadening of the phonon line. Since the values of λ extracted from fitting Raman lineshapes are sensitive to disorder for values of λ in the range of those found in $\text{YBa}_2\text{Ca}_3\text{O}_{7-\delta}$, a direct comparison with other compounds should again be considered qualitatively, with a view towards materials of comparable quality. Our Ewald calculations confirm that the field at the planar oxygen site for Bi-2212 ($E_z = 1.16 \text{ eV}/\text{\AA}$) is similar to $\text{YBa}_2\text{Cu}_3\text{O}_{7-\delta}$. We show in the next section that this value is likely underestimated once considerations for doping are taken into account.

B. Doping Dependence of the Electric Field

We now briefly comment on the doping dependence of the local crystal fields. In discussing the trends in E_z across the cuprates we have assumed formal valences for each lattice site, which is appropriate for undoped parent compounds. However, as was shown in Ref. 90, the doping process can significantly affect the strength of these fields resulting in a substantial local increase in λ 's. From a symmetry point of view, the movement of charge from the CuO_2 plane to the charge reservoir layers with increased doping will enhance local symmetry breaking

across plane. To model this effect in Bi-2212 we repeated the calculation for E_z , but this time with the charge of the CuO_2 planes uniformly raised by $0.15e$, corresponding to optimal doping. In order to maintain charge neutrality the charge of the BiO and SrO layers, where the O dopants are known to sit,¹¹⁰ were uniformly reduced by the appropriate amount. Using this crude model we find the E_z field at the planar site is raised to $3.56 \text{ eV}/\text{\AA}$ while the field at the apical site is reduced to $16.33 \text{ eV}/\text{\AA}$, in agreement with the general trends previously reported.⁹⁰ In section III we were interested in determining the values of $\lambda_{z,\phi}$ at optimal doping and therefore these are the values of the crystal field strength which were used in section III B to obtain the unscreened $\lambda_{z,\phi}(\mathbf{k})$ and total $\lambda_{z,\phi}$'s.

Throughout this paper we have discussed a number of aspects of el-ph coupling in the cuprates which are affected by doping the system. The local E -field strength, the ionicity of the compound, characterized by Ω_{pl} , and the orbital character of the band at the Fermi level all modify the el-ph couplings and are all affected by doping. Therefore, el-ph coupling in the cuprates is expected to exhibit a strong doping dependence. We also note that many of these parameters are also expected to vary between materials comprising the various families and we turn our attention to these trends in the following section.

C. Material Dependence of $\lambda_{z,\phi}$ for the B_{1g} branch

We end this section by examining the systematic variation in the el-ph coupling strength expected from material to material. Since our goal is to understand the materials variations in T_c we focus our attention on coupling to the B_{1g} branch, which provides the largest contribution to pairing and whose coupling is the strongest after the effects of screening are taken into account. As discussed previously, there is an empirical relationship between T_c and the distance of the apical oxygen from the CuO_2 plane and this relationship has generally been tied to the effective increase in the next nearest neighbour hopping t' through hybridization effects associated with the Cu $4s$ orbital. These hybridization effects will also alter the character of the $pd-\sigma^*$ band crossing the Fermi level and can therefore affect the overall strength of the coupling to all of the phonon branches considered in this work. For the B_{1g} branch, such changes are reflected in A_O and, since this enters the total coupling as the fourth power, changes in hybridization can have a large effect on the total coupling strength.

In Fig. 15a the systematic variation of A_O is presented as a function of T_c for the same materials considered in the Fig. 14. To estimate A_O we consider the same five-band model used in section III B, but assign the site energies based on the Madelung calculations presented here and the energy level scheme of Ref. 15. Using hole language, we set $\epsilon_d = 0$, $\epsilon_p = \Delta$, $\epsilon_a = \Delta + \Delta\Phi_A/\epsilon(\infty)$

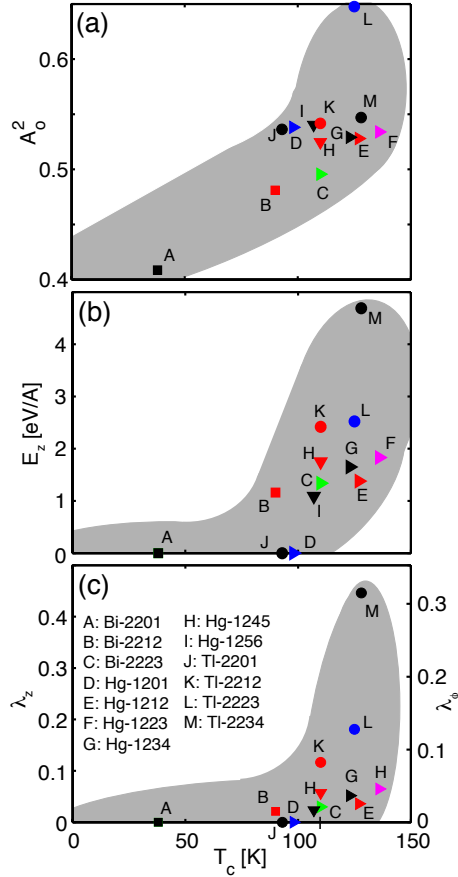


FIG. 15: (Color online) (a) The planar oxygen character at the Fermi surface A_O^2 as a function of the material's T_c . (b) The corresponding local E_z -field at the planar oxygen site of the outermost CuO_2 plane in the parent compound. (c) The value of λ_z for the B_{1g} modes of the outermost plane for each material.

and $\epsilon_s = \epsilon_d - 7$. Here, Δ is the charge transfer energy, which is related to the difference in Madelung energies between the Cu and planar O sites $\Delta\Phi_M = \Phi_O - \Phi_{Cu}$ and is given by

$$\Delta = \frac{\Delta\Phi_M}{\epsilon(\infty)} - I_{Cu}(2) + A_O(2) - \frac{e^2}{d_p} \quad (28)$$

where $I_{Cu}(2)$ and $A_O(2)$ are the second ionization and second electron affinity energies for the Cu and O sites, respectively. The factor of e^2/d_p represents the contribution of the Coulomb interaction between the introduced electron-hole pair. Following Ref. 15, we take the dielectric constant $\epsilon(\infty) = 3.5$ and $I_{Cu}(2) - A_O(2) + e^2/d_p = 10.9$ eV. In determining ϵ_a , $\Delta\Phi_A = \Phi_A - \Phi_O$ denotes the Madelung energy difference between the apical and planar oxygen sites. In addition to varying the site energies between materials, the values of the hoppings t'_{pp} and t'_{ps} are also adjusted using the prescription of Ref. 109. This allows us to account for changes in hybridization due to the different apical distance given in the experimental

structural data. Furthermore, we neglect any variation of the a and b lattice constants and hold the in-plane hybridizations fixed throughout. Finally, correlations are handled at the mean field level. The overall effect of the mean field corrections is to shift the site energies

$$\begin{aligned} \tilde{\epsilon}_d &= U_{dd}\langle n_i^d \rangle / 2 + 4U_{pd}\langle n_i^p \rangle + U_{pd}\langle n_i^a \rangle \\ \tilde{\epsilon}_p &= \epsilon_p + U_{pp}\langle n_i^p \rangle / 2 + 2U_{pd}\langle n_i^p \rangle \\ \tilde{\epsilon}_a &= \epsilon_a + U_{pp}\langle n_i^a \rangle / 2 + U_{pd}\langle n_i^d \rangle \end{aligned} \quad (29)$$

and $\tilde{\epsilon}_s$ is fixed to maintain the difference $\tilde{\epsilon}_d - \tilde{\epsilon}_s = 7$ eV. The Hubbard repulsions are set to canonical values with (in eV) $U_{dd} = 8$, $U_{pp} = 4$ and $U_{pd} = 1$. In Eq. (29), n_i^α denotes the total number operator for orbital α and site i and the paramagnetic solution for $\langle n_i^d \rangle$ has been assumed.

The results for A_O , E_z and $\lambda_{z,\phi}$ are shown in Fig. 15. The E_z -fields presented here are the same as those used in Fig. 14, and were obtained by assigning formal valences for each ion. These field values reflect best the crystal field of the undoped parent compounds and therefore Fig. 15 does not include the effects of doping. As we have already seen, even in this simple model, the redistribution of charge from the charge reservoir to the CuO_2 plane can alter the crystal field values resulting in large changes in the value of $\lambda_{z,\phi}$. In the case of Bi-2212 this produced an order of magnitude change in the value of $\lambda_{z,\phi}$ for the factor 4 change in E_z in the doped lattice. Furthermore, the ionic point charge model neglects any covalent nature of the bonds which will smooth the charge distributions. Therefore, the field strengths in real materials may be quite different from the values reported here, especially in the doped systems. However, by using the same method for each material we can obtain valuable comparative information about the crystal field variations between materials.

As shown in Fig. 15a, there is a correlation between the material's maximum T_c at optimal doping (apical distance) and the planar oxygen character A_O . Again, this can be understood in terms of the increase in the effective planar O-O hopping *via* the Cu $4s$ as the apical oxygen is further removed from the CuO_2 plane. A similar correlation, shown in Fig. 15b, occurs between E_z at the planar oxygen site and T_c for the reasons previously discussed. Since the total couplings $\lambda_{z,\phi}$ for the B_{1g} branch are proportional to the product $A_O^4 E_z^2$ a clear correlation between the material's T_c and the B_{1g} coupling naturally arises. This is shown in Fig. 15c.

The correlation between T_c and the strength of the coupling to the B_{1g} branch, which provides the largest contribution to d -wave pairing, provides a natural framework for thinking about materials variations in T_c . Although it is clear that the overall strength of the el-ph interaction is too small to support HTSC on its own,⁶⁴⁻⁶⁶ phonons are not precluded from contributing to pairing, enhancing the pairing correlations from another dominant interaction. Such a possibility has been considered in previous works that have examined the contribution

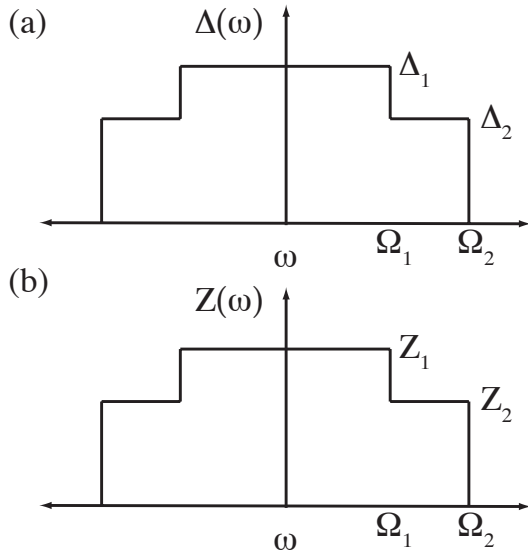


FIG. 16: The double square well model for $\Delta(\omega)$ and $Z(\omega)$.

of el-ph coupling in conjunction with antiferromagnetic spin fluctuations.^{111,112} In such a scenario, a baseline T_c is set by the dominant pairing mechanism, typically identified with antiferromagnetic spin fluctuations. Such an interaction is likely to be governed by the properties of the CuO_2 plane, such as the charge transfer energy Δ or antiferromagnetic exchange energy J , and therefore the strength of this interaction is likely independent of the material. T_c is then further enhanced by the weaker contribution from the el-ph interaction which, as we have shown, is strongly materials dependent. This picture naturally explains the variations in T_c that are observed across materials and provides a microscopic connection between the structure and composition of the unit cell and the T_c of the material.

In the next section we continue examine such a multi-channel model and present simplified considerations for T_c in order to assess the degree to which phonons can enhance a dominant interaction at high energy. As we will show, moderate values of $\lambda_{z,\phi}$, such as those given in Fig. 15c, can lead to sizeable enhancement to T_c which is greater than the T_c that would result from phonons alone. Phonons are therefore capable of providing a sufficiently large enhancement to T_c despite the relatively low value of their total coupling $\lambda_{z,\phi}$.

VI. CONSIDERATIONS OF MULTIPLE PAIRING CHANNELS: T_c AND THE ISOTOPE EFFECT

In this section we turn our attention to considerations for T_c by considering contributions to pairing from mul-

iple channels. T_c , one of the most difficult quantity to calculate correctly, varies across the cuprate families by two orders of magnitude even though the same CuO_2 building block is present. However, as we have demonstrated, the total el-ph coupling for the B_{1g} branch shows a strong materials dependence which is empirically correlated with the observed value of T_c at optimal doping. Therefore it is of interest to explore how el-ph interactions may provide a material dependence to T_c arising from the material conditions along the c -axis and poor screening.

To calculate T_c we consider a multi-channel boson exchange model for pairing, which is a straightforward generalization of the Eliashberg equations. A similar approach has recently been used¹¹³ to account for the qualitative structures in the phonon-modulated density of states of the cuprates as observed by STM.⁴⁵ Implicit in this calculation is the assumption that the dominant pairing channel can be described in terms of a boson exchange mechanism and such a scenario is the simplest one which can be adopted in examining the idea of phonon-enhanced HTSC. However, such a model can be perhaps be justified based on several recent works. For example, studies of the penetration depth in electron-doped cuprates using a model with coexisting AFM and SC order has produced good agreement with experiment indicating the importance of AFM in these systems.¹¹⁴ Furthermore, a DMFT study of optical conductivity in a moderately correlated single-band Hubbard model,¹¹⁵ has concluded that AFM with moderate correlations is the correct picture for describing the underdoped cuprates rather than strongly correlated Mott physics. Finally, a study of the t - J and Hubbard models has shown that the d -wave pairing in these models have a significant contribution from a retard component with an energy set by a few times J or a fraction of U in the t - J and Hubbard models, respectively.¹¹⁶ This result indicates that the pairing interaction in these models is largely retarded in nature with an energy scale set by the dynamics of the magnetic excitation spectrum. These theoretical studies lend some support to the spin-fluctuation mediated picture adopted here although the details may differ. Nevertheless, this model provides a simple means to evaluate the role of phonons in modifying T_c in a multi-channel model.

For this calculation we assume that each channel can be described in terms of a boson exchange mechanism. Individual channels are indexed by ν and the el-boson contributions to the mass renormalization $Z(\omega)$ and anomalous self-energy $\phi(\theta, \omega)$ are parameterized by $\lambda_{\nu,z}$ and $\lambda_{\nu,\phi}$, respectively. Making the standard approximations of a structureless band and cylindrical Fermi surface, the multi-channel Eliashberg equations are

$$\begin{aligned}
\omega[1 - Z(\omega)] &= \sum_{\nu} \frac{\lambda_{\nu,z}\Omega_{\nu}}{2} \int_0^{\infty} d\omega' \left\langle \frac{\omega'}{\sqrt{\omega'^2 - \Delta^2(\omega) \cos^2(2\theta)}} \right\rangle K_{+}^{\nu}(\omega', \omega) \\
\Delta(\omega)Z(\omega) &= \sum_{\nu} \frac{\lambda_{\nu,\phi}\Omega_{\nu}}{2} \int_0^{\infty} d\omega' \left\langle \frac{\Delta(\omega') \cos^2(2\theta)}{\sqrt{\omega'^2 - \Delta^2(\omega') \cos^2(2\theta)}} \right\rangle K_{-}^{\nu}(\omega', \omega).
\end{aligned} \tag{30}$$

Here we have assumed a separable form for the anomalous self-energy $\phi(\theta, \omega) = \phi(\omega) \cos(2\theta)$ and $\Delta(\omega) = \phi(\omega)/Z(\omega)$ is the complex gap function. The kernels in Eq. (30) are given by

$$K_{\pm}^{\nu}(\omega', \omega) = [f(-\omega') + n(\Omega_{\nu})] \left[\frac{1}{\omega + \Omega_{\nu} + \omega'} \pm \frac{1}{\omega - \Omega_{\nu} - \omega'} \right] + [f(\omega') + n(\Omega_{\nu})] \left[\frac{1}{\omega - \Omega_{\nu} + \omega'} \pm \frac{1}{\omega + \Omega_{\nu} - \omega'} \right]$$

where f and n are the Fermi and Bose occupation factors, respectively. Following Ref. 111 we adopt a double square-well model for the frequency dependence of $\Delta(\omega)$ and $Z(\omega)$, as shown in Fig. 16. Here, we identify $\nu = 1$ with the $\Omega_1 \sim 35$ meV B_{1g} phonon branch, and $\nu = 2$ is identified with antiferromagnetic spin fluctuations with $\Omega_2 = 2J \sim 260$ meV, reflecting the top of the magnon band in the case of a long-range antiferromagnet. Next, we follow a standard set of approximations¹¹⁷ and obtain the coupled equations

$$Z_1 \Delta_1 = (\lambda_{1,\phi} + \lambda_{2,\phi}) \int_0^{\Omega_1} d\omega' \frac{\Delta_1}{\omega'} \tanh\left(\frac{\omega'}{2k_b T_c}\right) + (\lambda_{1,\phi} + \lambda_{2,\phi}) \int_{\Omega_1}^{\Omega_2} d\omega' \frac{\Delta_2}{\omega'} \tanh\left(\frac{\omega'}{2k_b T_c}\right) \tag{31}$$

for $\Omega_1 > \omega \geq 0$ and

$$Z_2 \Delta_2 = \lambda_{2,\phi} \int_0^{\Omega_1} d\omega' \frac{\Delta_1}{\omega'} \tanh\left(\frac{\omega'}{2k_b T_c}\right) + \lambda_{2,\phi} \int_{\Omega_1}^{\Omega_2} d\omega' \frac{\Delta_2}{\omega'} \tanh\left(\frac{\omega'}{2k_b T_c}\right) \tag{32}$$

for $\Omega_2 \geq \omega \geq \Omega_1$. Here $Z_1 = 1 + \lambda_{1,z} + \lambda_{2,z}$ and $Z_2 = 1 + \lambda_{2,z}$.

Eqs. (32) and (31) are then solved for the non-trivial solution for Δ_i and the resulting expression for T_c is

$$k_B T_c = 1.134 \hbar \Omega_1^{1-\gamma} \Omega_2^{\gamma} \exp\left(-\frac{1 + \lambda_{1,z} + \lambda_{2,z}}{\lambda_{1,\phi} + \lambda_{2,\phi}}\right) \tag{33}$$

where

$$\gamma = \frac{\lambda_{2,\phi}}{1 + \lambda_{2,z}} \frac{1 + \lambda_{1,z} + \lambda_{2,z}}{\lambda_{1,\phi} + \lambda_{2,\phi}} \tag{34}$$

This expression recovers the McMillan result (we have neglected μ^*) for the single well case in either limit when $\lambda_{1,z}, \lambda_{1,\phi}$ or $\lambda_{2,z}, \lambda_{2,\phi}$ are set to zero. Other expressions have been obtained for T_c using different forms of the two-well model and neglecting the difference in contributions from each of the momentum channels (i.e. $\lambda_z = \lambda_{\phi}$) while taking the spin-fluctuation contribution to be repulsive.^{118–120} We refer the reader to Ref. 120 for a more thorough discussion of the various proposed expressions.

In order to assess the phonon contribution to T_c , we now assume that spin-fluctuations provide the dominant source for d -wave pairing and parameterize this mode with $\lambda_{2,z} = 2\lambda_{2,\phi} = 1$. This choice results in a baseline

$T_c = 62$ K in the absence of phonons. For the phonon mode we assume $\Omega_1 = 36$ meV and hold $\lambda_{1,z} = 2\lambda_{1,\phi}$. In Fig. 17a the resulting T_c as a function of el-ph coupling is presented. For reference, the value of T_c obtained from phonons alone is also shown, multiplied by a factor of 10. It is important to note that even small el-ph coupling can enhance T_c considerably over the single-channel spin fluctuation model. Furthermore, the degree of enhancement depends on the ratio of $\lambda_{2,\phi}/\lambda_{2,z}$ assumed for the spin fluctuations. In Fig. 17b we plot T_c for the two-mode model while varying ratios of $\lambda_{2,\phi}/\lambda_{2,z}$. In each case we have adjusted $\lambda_{2,\phi}$ such that the baseline of $T_c = 62$ K is maintained for $\lambda_{1,\phi} = 0$. In general, as $\lambda_{2,\phi}/\lambda_{2,z}$ increases in the dominant channel, the overall gain in T_c mediated by phonons also increases but with diminishing returns for larger $\lambda_{2,\phi}/\lambda_{2,z}$. An isotropic repulsion in the spin fluctuation channel is also expected to produce a similar effect. We also note that our results are limited by the questionable applicability of Migdal-Eliashberg theory in the cuprates and therefore T_c itself is a poor metric of a theory to be compared to experiment. Nevertheless, as this enhancement is generic to multi-channel couplings, it may serve as a guide for un-

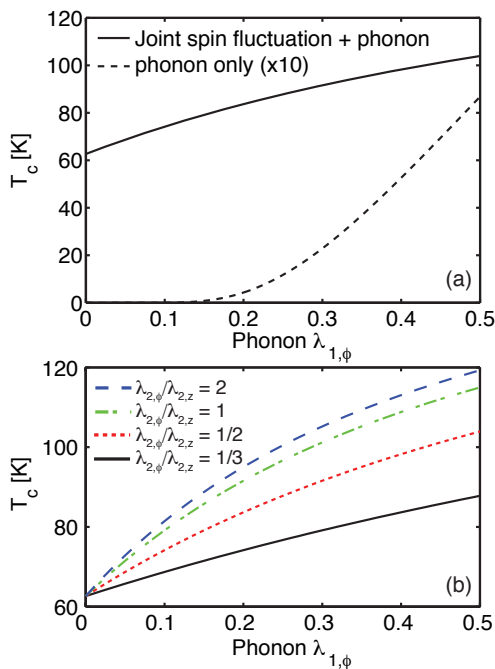


FIG. 17: The transition temperature T_c as a function of el-ph coupling in the d -wave channel $\lambda_{1,\phi}$, calculated in the two-square well model, defined in the text. The dashed line is T_c expected for the phonon alone.

derstanding the material dependence of T_c itself.

In Fig. 18 the isotope exponent $\alpha = -\partial \ln T_c / \partial \ln M$, where M is the mass of the oxygen ion, is plotted using the same parameters as in Fig. 17 with $\alpha = (1-\gamma)/2$, and γ defined by Eq. (34), reducing the overall magnitude of α from the value for phonons alone. A similar reduction in α and enhancement of T_c has been reported in Ref. 112 when the phonon contribution to pairing was taken to be attractive in the $d_{x^2-y^2}$ channel. Fig. 18 shows that the overall isotope exponent is small even though the phonon mediated enhancement to T_c is sizeable and demonstrates that small isotope exponents are possible despite large enhancements in T_c due to the el-ph interaction.

Some degree of caution is warranted in making a direct comparison to experiment where the isotope exponent is small at optimal doping and increases with underdoping,²¹ while our results show that the overall contribution of el-ph coupling to d -wave pairing is expected to increase with doping due to screening effects. Therefore one might expect that the isotope exponent should increase with doping, contrary to what has been observed experimentally. However, doping dependent changes are also likely to occur for a spin-fluctuation mediated pairing mechanism. Since it is the relative contributions from each channel that sets the value of α a direct calculation of α expected experimentally is not possible until the details of the dominate pairing interaction are understood. Nevertheless, these calculations show that

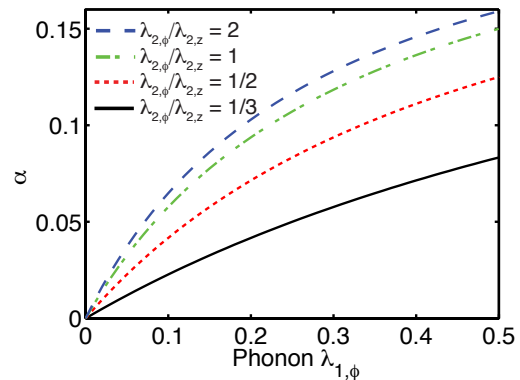


FIG. 18: The isotope exponent α as a function of el-ph coupling $\lambda_{1,\phi}$ for the same parameter set used in Fig. 17.

phonons with relatively low el-ph coupling strengths can, in principle, play a substantial role in determining T_c while producing small signatures in traditional metrics such as the isotope exponent.

We end with a few comments about these results in relation to prior works. As we have already noted, the specific results presented are limited by the applicability of Eliashberg theory and the Fermi liquid description of the cuprates. Such a picture may not be completely applicable, especially in the underdoped region of the phase diagram where the role of correlations becomes more prominent. As the role of correlations and its interplay with the el-ph interaction is better understood the details of the picture presented here may change. However, the phonon-mediated enhancement of T_c is expected remain as a general phenomenon.

We also note that the inclusion of correlations may further enhance the phonon contribution to T_c through possible enhancements of the el-ph vertex or proximity to AFM. For example, Recent DMFT work examining phonon-mediated pairing in the fullerenes^{121,122} has found that a phonon-mediated pairing mechanism, which produces an exponentially small T_c when considered on its own, will be significantly enhanced in proximity to a metal-insulator transition. The mechanism via which this occurs is a density of states enhancement due to a narrowing of the quasi-particle band and Mott physics. This is a different origin than the enhancement reported here where we are concerned with the overall effects of coherence and band width of the paired electrons. Some aspects of the Mott physics is included in our considerations in the form of the breakdown of metallic screening along the c -axis (a Coulomb effect) however, we have not included the breakdown of carrier properties in the CuO_2 plane. This is an intriguing possibility but it is beyond the scope of our paper and we leave it for future work.

Finally, it has recently shown that high values of T_c are also obtainable from el-ph coupling without invoking a second dominant pairing interaction by departing from the conventional Fermi liquid framework. In Ref. 123 it

was shown that T_c 's on the order of 100 K are attainable for $\lambda_{z,\phi}$ values similar to those obtained here, provided the normal state behaves as a non-Fermi-liquid quantum critical metal. Although the simple approach outlined here does not hold in this scenario, much of the doping and materials-dependent variations in coupling still do.

VII. SUMMARY AND CONCLUSIONS

Although there appears to be a great deal of universality in the hole-doped cuprates, large changes in T_c can be achieved through changes in the chemical composition and structure of the unit cell. As we have shown here, these changes are reflected in a number of properties including the orbital character of the band crossing the Fermi level, the strength of local electric fields arising from structural-induced symmetry breaking, doping dependent changes in the underlying band structure, and ionicity of the crystal governing its ability to screen c -axis perturbations. Given the sensitivity of T_c to the structural details of the crystal it is clear that the underlying mechanism(s) for HTSC must incorporate these elements in some way. In this work we have examined a number of aspects of coupling to oxygen modes and demonstrated that the overall coupling to these modes is quite sensitive to these factors. Therefore, the inclusion of el-ph coupling to these modes provides a natural means of linking the electronic properties of the CuO_2 plane to the structural elements of the material lying off plane and the carrier concentration. This picture calls for oxygen phonons to play a role in HTSC.

In extending the previous works by some of the authors on el-ph coupling in the cuprates, we have formulated a theory for poor screening in these materials. Due to the quasi-2D nature of the cuprates with poor conductivity along the c -axis, we have shown that a window of small \mathbf{q} opens in which screening is inoperable. This results in an overall enhancement of the total d -wave projected coupling which enhances the phonon's ability to mediate d -wave pairing. With progressive doping, the total phonon contribution to λ_ϕ is enhanced while the total contribution from λ_z , which suppresses d -wave pairing, is screened away. As a result, doping the system away from half-filling results in an increased contribution to d -wave superconductivity mediated by el-ph coupling.

A systematic examination of the variation in el-ph coupling across the cuprate families was also performed. Using experimental structural data we determined the materials variation in the total electric field strength and orbital character of the $pd\text{-}\sigma^*$ band at the Fermi level and the expected variations in el-ph coupling strength to the B_{1g} branch. A direct correlation between the strength of the coupling and the optimal T_c for each material was observed. As a result, the materials variation in T_c can be naturally accounted for through the inclusion of el-ph coupling to the presently accepted intrinsic planar models.

To be clear, we do not suggest that el-ph coupling alone accounts for HTSC as both the bare and screened values for the el-ph coupling strength are insufficient to produce large T_c 's on their own. Instead, we propose that the phonons work in conjunction with the presently unidentified dominant mechanism for HTSC. The simplified multi-channel model for T_c presented here has demonstrated that moderate el-ph coupling, when combined with spin fluctuations, can produce enhancements to the total T_c in excess of the contribution produced by phonons alone. Furthermore, this enhancement is expected to be a generic phenomena and independent of the presently second mechanism. Therefore, the inclusion of the el-ph interaction can account for the large variations in T_c observed across the cuprate as a function of material and doping.

There are some open issues regarding el-ph coupling in the cuprates. First of all, our examination of the field strength as a function of material neglected any doping-induced changes to the field strengths. Our simplified treatment of the bi-layer system Bi-2212 showed that these effects can be substantial. Therefore, this problem requires a systematic examination of the doping process across the families of cuprates, perhaps with more sophisticated approaches. This issue is complicated in the multi-layer systems with $n > 2$ where there is the possibility for inequivalent dopings for the CuO_2 planes.⁴⁹ This can further modify charge distributions altering the strength of the crystal fields in each plane.⁵⁵ Any systematic treatment of the doping induced fields should take this into account. There is also the additional question of the role of covalency in determining the overall field strength.

Finally, we have investigated the role of el-ph coupling in the cuprates, taking into account the long range Coulomb interaction and its role in screening. However, the role of the short-range Coulomb interaction and its affect on the el-ph interaction remains an open and intriguing question. We believe that the findings presented in this paper serve to further highlight the need for progress in this area.

Acknowledgments

The authors would like to acknowledge useful discussions with A. Balatsky, O. Gunnarsson, G. Sangiovanni, I. Mazin, R. Hackl and D. J. Scalapino. T. P. D. would like to acknowledge support from NSERC, ONR grant N00015-05-1-0127 and the A. von Humboldt Foundation. The Stanford work is also supported by DOE contract DE-AC03-765F00515, NSF grant DMR-0304981 and ONR grant N00014-01-1-0048. S. J. would like to acknowledge support from NSERC and SHARCNET. N. N. is supported by the Grant-in-Aids for Scientific Research (No. 17105002, 19019004, 19048008, 19048015, and 21244053) from the Ministry of Education, Culture, Sports, Science and Technology of Japan, and also by

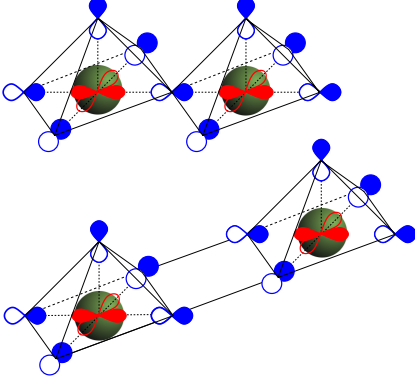


FIG. 19: (Color online) Cu_2O_9 and Cu_2O_{10} clusters used to compute the modifications of the effective Zhang-Rice singlet hopping t and t' and magnetic coupling J and J' .

Funding Program for World-Leading Innovative R&D on Science and Technology (FIRST Program)

Appendix A: Modifications of the Zhang-Rice Singlet

Throughout this work the role of electronic correlations was neglected in deriving the anisotropic el-ph couplings arising from different charge transfer processes. In this appendix an analysis via a different route is undertaken by examining directly the role played by correlations. Previous studies on Hubbard clusters have illustrated the usefulness of exact diagonalization for exploring low energy excitations, such as the Zhang-Rice singlet (ZRS),¹²⁴ as a function of hole number. In particular, these studies have demonstrated a strong dependence of the ZRS energy and mobility, as well as the magnetic exchange J , on the planar charge transfer energy $\Delta = \epsilon_p - \epsilon_d$.¹²⁵ Ref. 15 pointed out that the stability of the ZRS increases if the apical atom lies further away from the CuO_2 plane, which reduces the mixing of the ZRS with other low energy states of the cluster. Since the phonons under consideration directly modulate Δ and the apical Madelung energy, strong modifications should be seen in the ZRS and magnetic exchange. The cell perturbation approach in Ref. 126, which included in-plane oxygen breathing and buckling modes, showed that an effective simple Hubbard-like Hamiltonian can be deduced with renormalized parameters.

Here, exact diagonalization studies of multi-band Hubbard clusters are used to investigate how the low energy sector is modified by local, static atomic displacements in a pattern given by various phonon eigenvectors. The modifications of the ZRS and J due to el-ph coupling receive close attention in order to derive renormalized parameters for single-band Hubbard to t - J model Hamiltonians.

The clusters show in Fig. 19 contain two sets of orbitals at the Cu site: $3d_{x^2-y^2}$ and $4s$. By symmetry, the

hopping amplitude from the apical oxygen site to the Cu $3d_{x^2-y^2}$, t_{ad} vanishes, while t_{as} is non-zero. Thus, a general Hubbard model can be written as $H = H_{kin} + H_{pot}$ where the kinetic piece is

$$\begin{aligned}
 H_{kin} &= t_{pd} \sum_{i,\sigma} Q_\delta [d_{i,\sigma}^\dagger p_{i,\delta,\sigma} + h.c.] \\
 &+ t_{pp} \sum_{i,\delta,\delta',\sigma} Q'_{\delta,\delta'} p_{i,\delta,\sigma}^\dagger p_{i,\delta',\sigma} \\
 &+ t_{ap} \sum_{i,\delta,\sigma} Q''_\delta [a_{i,\sigma}^\dagger p_{i,\delta,\sigma} + h.c.] \\
 &- t_{as} \sum_{i,\sigma} [a_{i,\sigma}^\dagger s_{i,\sigma} + h.c.] \\
 &- t_{ps} \sum_{i,\sigma} Q''_\delta [s_{i,\sigma}^\dagger p_{i,\delta,\sigma} + h.c.] \quad (\text{A1})
 \end{aligned}$$

with phase factors $Q_{\pm x} = -Q_{\pm y} = \mp 1$, $Q'_{\pm x, \pm y} = 1 = Q'_{\pm x, \mp y}$, $Q''_{\pm x} = Q''_{\pm y} = \pm 1$, and the potential piece is given by

$$\begin{aligned}
 H_{pot} &= U_{dd} \sum_i \hat{n}_{i,\uparrow}^d \hat{n}_{i,\downarrow}^d + U_{pp} \sum_{i,\delta} \hat{n}_{i,\delta,\uparrow}^p \hat{n}_{i,\delta,\downarrow}^p \\
 &+ \epsilon_d \sum_{i,\sigma} \hat{n}_{i,\sigma}^d + \epsilon_s \sum_{i,\sigma} \hat{n}_{i,\sigma}^s \\
 &+ \sum_{i,\sigma} (\epsilon_a + \vec{U}_a \cdot \vec{E}_a) \hat{n}_{i,\sigma}^a \\
 &+ \sum_{i,\delta,\sigma} (\epsilon_p + \vec{U}_{i,\delta} \cdot \vec{E}_p) \hat{n}_{i,\sigma}^a. \quad (\text{A2})
 \end{aligned}$$

Here, a , p_δ , d , s ($a^\dagger, p_\delta^\dagger, d^\dagger, s^\dagger$) annihilate (create) a hole on apical oxygen, in-plane oxygen ($\delta = x, y$), copper d - and copper s -orbital, respectively, \vec{U} is the displacement of a given ion and \vec{E} is the associated local electronic field. This type of coupling is different than that considered in previous studies, where the buckling modes were represented as an electrostatic modulation of the Cu site energies.¹²⁶ Since the $4s$ orbitals are rather extended we neglect the on-site Coulomb repulsion as well as inter-orbital interactions with the $3d_{x^2-y^2}$ orbitals.

There are a total of 13 and 14 orbitals for the Cu_2O_9 and Cu_2O_{10} clusters, respectively. In both cases, the clusters contain seven holes in order to investigate the formation and delocalization of a ZRS to a nearest neighbour copper-oxide plaquette (4 holes being almost exclusively located in the Cu $4s$ orbitals). Exact diagonalizations in the $S_{tot}^z = 1/2$ sector, which contains the ground state, are performed since the Hamiltonian conserves S_{tot}^z . Parameters similar to those of Ref. 15 for the Hubbard model are used, with values representative of the electric field for the planar and apical oxygen sites

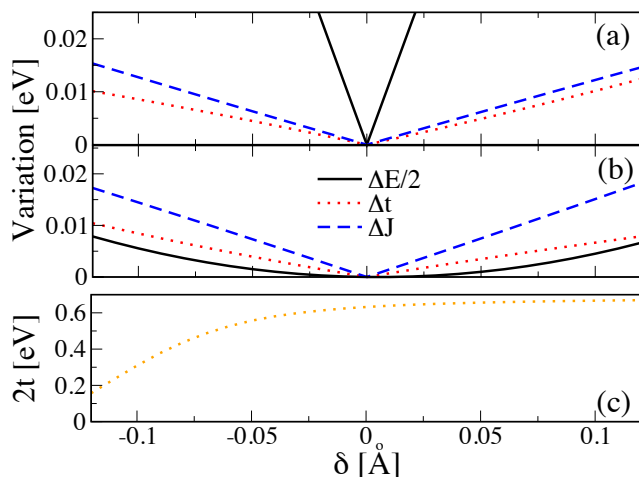


FIG. 20: (Color online) The effect of different modes on various Zhang-Rice parameters for the Cu_2O_9 cluster: plots (a) and (b) show the effect of a given mode on the ground-state energy and on the effective ZRS hopping t with $\Delta t = |t(\delta) - t(\delta = 0)|$ and $\Delta E = E(\delta) - E(\delta = 0)$. (a) The effect of the A_{1g} modes. (b) The effect of the B_{1g} mode. (c) The effect of the apical mode on $2t$.

in bilayer cuprates (in eV and eV/Å for the fields):

$$\begin{aligned}
 t_{pd} &= 1.13 & t_{ps} &= 2 \\
 t_{pp} &= 0.49 & t_{ap} &= 0.29 \\
 t_{as} &= 2 & \epsilon_s &= -7 \\
 \epsilon_p &= \epsilon_a = 2.9 & U_{pp} &= 4.1 \\
 U_{dd} &= 8.5 & E_p &= 1.6 \\
 & & E_a &= 16
 \end{aligned}$$

The diagonalization of the Cu_2O_9 cluster yields the effective hopping parameter t of the ZRS as well as the magnetic exchange J : the splitting between the ground-state and first excited state gives $2t$, whereas the singlet-triplet splitting of the 6-particle problem gives J . The parameters t' and J' are analogously defined from the Cu_2O_{10} cluster. In the absence of el-ph coupling we obtain the following values: $|2t| = 0.63$ eV, $|2t'| = 0.28$ eV, $J = 0.17$ eV, and $J' = 15$ meV.

Fig. 20 displays the effect of different phonon modes on the ground state energy, t and J as a function of static displacement δ . Although only static atomic displacements have been investigated in configurations corresponding to the phonon eigenvectors, the differences between the relevant time scales associated with the electron hopping and atomic motion justify such an analysis for the purpose of viewing a snap-shot of the modifications of the ZRS parameters. (We also note that Ref. 90 considered a similar calculation with fully quantized atomic motion for the B_{1g} and A_{1g} phonons at $\mathbf{q} = 0$ and reported similar results for J .) One clearly sees, for small displacements, the main effect on t is due to the A_{1g} and B_{1g} modes. For the B_{1g} mode, the effective

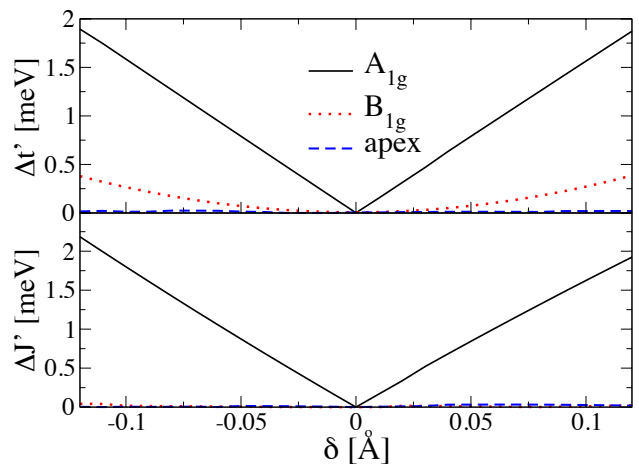


FIG. 21: (Color online) Variation of the effective Zhang-Rice hopping t' and magnetic exchange J' to next-nearest neighbor. The calculation performed for the Cu_2O_{10} cluster for A_{1g} -, B_{1g} - and apex-modes.

hopping of the ZRS is modulated to first order in the displacement, while the energy is only modified at second order, in agreement with perturbative analysis. For the A_{1g} mode the first-order correction to the energy does not vanish and both ΔE and $\Delta t \propto \delta$. The magnitude of the modulation in t is comparable to the B_{1g} mode with the same local field. The effect of the apical mode on t is very weak for $\delta > 0$. This is not surprising since the ZRS has little apical character if the orbital lies away from the CuO_2 plane. For $\delta < 0$ the hybridization of the apical- p and $\text{Cu}-d_{3z^2-r^2}$ orbitals destabilizes the ZRS and thus the effective hopping t drops as in an earlier work.¹⁵ Also, both the ground state energy E and the effective exchange J are not affected much by this mode.

It is clear, based on the calculations performed, that the three modes modify the effective hopping of the ZRS. However, the mechanism by which the apical mode affects the hopping is very different since the formation of the ZRS no longer takes place in the CuO_2 plane if the displacement of the apical oxygen is towards the plane. The effective next-nearest neighbour quantities t' and J' (see Fig. 21) are affected less by the two planar modes.

Summarized in Figs. 20 and 21, our results indicate that for both the A_{1g} and B_{1g} phonons, Δt as well as ΔJ corrections have a linear dependence on displacement of about the same magnitude. For the apical phonon the magnitude is different due to the destabilization of the ZRS. The on-site energy is modified mainly by the A_{1g} ep-ph coupling; which can be quantified by looking at the corresponding modification of the ground-state energy. Modifications to parameters $\Delta J'$ and $\Delta t'$ indicate again that the dominant contribution comes from the A_{1g} mode. However, this conclusion is based on a naive cluster approach and should be corroborated by other means of investigation.

In terms of treatments of effective single-band models,

such as Hubbard or t - J , incorporating phonons, we note that our results indicate that the effective couplings for these modes are neither purely Holstein-like nor can they be treated as bond phonons simply modifying the effective ZRS hopping t : the effective parameters, such as t and J , and as a consequence, the Mott-Hubbard effective interaction U in a single-band approach, are all modified. The actual modification of the effective U for static

displacements corresponding to these phonon modes requires an investigation of different three-band clusters containing Cu d^8 , d^9 and d^{10} and oxygen ligand configurations. This points out the complications involved in ascribing real phonon modes to any corresponding model phonons in a single-band approach, and illustrates the important interplay between el-ph coupling and electronic correlations.

-
- ¹ See, e.g., D. J. Scalapino, *Handbook of High-Temperature Superconductivity*, ed. J. R. Schrieffer, Springer (2006); arXiv:cond-mat/0610710.
- ² M. Gurvitch and A. T. Fiory, Phys. Rev. Lett. **59**, 1337 (1987); S. Martin, A. T. Fiory, R. M. Fleming, L. F. Schneemeyer and J. V. Waszczak, Phys. Rev. B **41**, 846 (1990).
- ³ S. Komiyama, Y. Ando, X. F. Sun and A. N. Lavrov, Phys. Rev. B **65**, 214535 (2002).
- ⁴ E. Pavarini, I. Dasgupta, T. Saha-Dasgupta, O. Jepsen and O. K. Andersen, Phys. Rev. Lett. **87**, 047003 (2001).
- ⁵ L. Spanu, M. Lugas, F. Becca and S. Sorella, Phys. Rev. B **77**, 024510 (2008).
- ⁶ E. Khatami, A. Macridin, and M. Jarrell, Phys. Rev. B **78**, 060502(R) (2008).
- ⁷ C. T. Shih, T. K. Lee, R. Eder, C.-Y. Mou and Y. C. Chen, Phys. Rev. Lett. **92**, 227002 (2004).
- ⁸ P. W. Anderson, Science **268**, 1154 (1995); S. Chakravarty, H.-Y. Kee and E. Abrahams, Phys. Rev. Lett. **82**, 2366 (1999).
- ⁹ D. van der Marel and J. H. Kim, J. Phys. Chem. Sol. **56**, 1825 (1995).
- ¹⁰ A. A. Tsvetkov, D. van der Marel, K. A. Moler, J. R. Kirtley, J. L. de Boer, A. Meetsma, Z. F. Ren, N. Kolshnikov, D. Dulic, A. Damascelli, M. Grüninger, J. Schützmann, J. W. van der Eb, H. S. Somal and J. H. Wang, Nature **395**, 360 (1998).
- ¹¹ K. McElroy, J. Lee, J. A. Slezak, D.-H. Lee, H. Eisaki, S. Uchida and J. C. Davis, Science **309**, 1048 (2005).
- ¹² T. S. Nunner, B. M. Andersen, A. Melikyan and P. J. Hirschfeld, Phys. Rev. Lett. **95**, 177003 (2005); T. S. Nunner, W. Chen, B. M. Andersen, A. Melikyan and P. J. Hirschfeld, Phys. Rev. B **73**, 104511 (2006); J.-X. Zhu, K. McElroy, J. Lee, T. P. Devereaux, Q. Si, J. C. Davis, A. V. Balatsky, Phys. Rev. Lett. **97**, 177001 (2006); R. Jamei, J. Robertson, E.-A. Kim, A. Fang, A. Kapitulnik and S. A. Kivelson, Phys. Rev. B **74**, 174521 (2006).
- ¹³ K. Fujita, T. Noda, K. M. Kojima, H. Eisaki and S. Uchida, Phys. Rev. Lett. **95**, 097006 (2005); H. Eisaki, N. Kaneko, D. L. Feng, A. Damascelli, P. K. Mang, K. M. Shen, Z.-X. Shen and M. Greven, Phys. Rev. B **69**, 064512 (2004).
- ¹⁴ W. B. Gao, Q. Q. Liu, L. X. Yang, Y. Yu, F. Y. Li, C. Q. Jin, S. Uchida, Phys. Rev. B **80**, 094523 (2009).
- ¹⁵ Y. Ohta, T. Tohyama and S. Maekawa, Phys. Rev. B **43**, 2968 (1991); C. Di Castro, L. F. Feiner and M. Grilli, Phys. Rev. Lett. **66**, 3209 (1991); J. H. Jefferson, H. Eskes, and L. F. Feiner, Phys. Rev. B **45**, 7959 (1992); L. F. Feiner, M. Grilli and C. Di Castro, Phys. Rev. B **45**, 10647 (1992); R. Raimondi, J. H. Jefferson and L. F. Feiner, Phys. Rev. B **53**, 8774 (1996).
- ¹⁶ A. Iyo, Y. Tanaka, M. Tokumoto and H. Ihara, Physica C **366**, 43 (2001); A. Iyo, M. Hirai, K. Tokiwa, T. Watanabe and Y. Tanaka, Supercond. Sci. Technol. **17**, 143 (2004).
- ¹⁷ Y. Chen, A. Iyo, W. Yang, X. Zhou, D. Lu, H. Eisaki, T. P. Devereaux, Z. Hussain and Z.-X. Shen, Phys. Rev. Lett. **97**, 236401 (2006); W. Xie, O. Jepsen, O. K. Andersen, Y. Chen and Z.-X. Shen, Phys. Rev. Lett. **98**, 047001 (2007).
- ¹⁸ A. Damascelli, Z. Hussain and Z.-X. Shen, Rev. Mod. Phys. **75**, 473 (2003).
- ¹⁹ See, e.g., A. S. Alexandrov and N. F. Mott, *High Temperature Superconductors and other Superfluids*, Taylor and Francis, 1994.
- ²⁰ J. G. Bednorz and K. A. Müller, Z. Phys. B **64**, 189 (1986).
- ²¹ B. Batlogg, R. J. Cava, A. Jayaraman, R. B. van Dover, G. A. Kourouklis, S. Sunshine, D. W. Murphy, L. W. Rupp, H. S. Chen, A. White, K. T. Short, A. M. Mujsce and E. A. Rietman, Phys. Rev. Lett. **58**, 2333 (1987); L. C. Bourne, M. F. Crommie, A. Zettl, H. C. zur Loye, S. W. Keller, K. L. Leary, A. M. Stacy, K. J. Chang and M. L. Cohen, Phys. Rev. Lett. **58**, 2337 (1987); P. J. Yvon, R. B. Schwarz, C. B. Pierce, L. Bernardez, A. Conners, and R. Meisenheimer, Phys. Rev. B **39**, 6690, (1989).
- ²² L. Perfetti, P. A. Loukakos, M. Lisowski, U. Bovensiepen, H. Eisaki and M. Wolf, Phys. Rev. Lett. **99**, 197001 (2007).
- ²³ S. Y. Savrasov and O. K. Andersen, Phys. Rev. Lett. **77**, 4430 (1996); S. Y. Savrasov, D. Y. Savrasov and O. K. Andersen, Phys. Rev. Lett. **72**, 372 (1994).
- ²⁴ O. K. Andersen, S. Y. Savrasov, O. Jepsen and A. I. Liechtenstein, Journ. Low Temp. Phys. **105**, 285 (1996); O. Jepsen, O. K. Andersen, I. Dasgupta and S. Savrasov, J. Phys. Chem. Solids **59**, 1718 (1998).
- ²⁵ T. Sakai, D. Poilblanc and D. J. Scalapino, Phys. Rev. B **55**, 8445 (1997).
- ²⁶ M. Capone, G. Sangiovanni, C. Castellani, C. Di Castro and M. Grilli, Phys. Rev. Lett. **92**, 106401 (2004).
- ²⁷ B. J. Alder, K. J. Runge and R. T. Scalettar, Phys. Rev. Lett. **79**, 3022 (1997).
- ²⁸ G. Sangiovanni, M. Capone, C. Castellani and M. Grilli, Phys. Rev. Lett. **94**, 026401 (2005).
- ²⁹ G. Sangiovanni, O. Gunnarsson, E. Koch, C. Castellani and M. Capone, Phys. Rev. Lett. **97**, 046404 (2006).
- ³⁰ P. Werner and A. J. Millis, Phys. Rev. Lett. **99**, 146404 (2007).
- ³¹ O. Rösch and O. Gunnarsson, Phys. Rev. Lett. **92**, 146403 (2004); A. S. Mishchenko and N. Nagaosa, Phys. Rev. Lett. **93**, 036402 (2004); O. Gunnarsson and O. Rösch, Phys. Rev. B **73**, 174521 (2006); P. Prelovšek, R. Zeyher and P. Horsch, Phys. Rev. Lett. **96**, 086402 (2006). *id.* J. Phys.: Condens. Matter **20**, 043201 (2008); A.

- S. Mishchenko, *Adv. Cond. Matt. Phys.* **2010**, 306106 (2010);
- ³² O. Rösch and O. Gunnarsson, *Phys. Rev. B* **70**, 224518 (2004).
- ³³ J. Bonča, S. Maekawa, T. Tohyama and P. Prelovšek, *Phys. Rev. B* **77**, 054519 (2008).
- ³⁴ Z. B. Huang, W. Hanke, E. Arrigoni and D. J. Scalapino, *Phys. Rev. B* **68**, 220507(R) (2003).
- ³⁵ M. L. Kulić and R. Zeyher, *Phys. Rev. B* **49**, 4395 (1994); R. Zeyher and M. L. Kulić, *ibid.* **53**, 2850 (1996);
- ³⁶ S. Ishihara and N. Nagaosa, *Phys. Rev. B* **69**, 144520 (2004).
- ³⁷ E. Koch and R. Zeyher, *Phys. Rev. B* **70**, 094510 (2004).
- ³⁸ R. Citro, S. Cojocaru and M. Marinaro, *Phys. Rev. B* **72**, 115108 (2005).
- ³⁹ A. Macridin, B. Moritz, M. Jarrell and T. Maier, *Phys. Rev. Lett.* **97**, 056402 (2006); A. Macridin, B. Moritz, M. Jarrell and T. Maier, *arXiv:cond-mat/0611067* (2006).
- ⁴⁰ V. I. Anisimov, M. A. Korotin, J. Zaanen and O. K. Andersen, **68**, 345 (1992).
- ⁴¹ J. Zaanen and P. B. Littlewood, *Phys. Rev. B* **50**, 7222 (1994).
- ⁴² For a review, see e.g., T. Cuk, D. H. Lu, Z.-J. Zhou, Z.-X. Shen, T. P. Devereaux and N. Nagaosa, *Phys. Stat. Sol. (b)* **242**, 11 (2005).
- ⁴³ A. Lanzara, P. V. Bogdanov, X. J. Zhou, S. A. Kellar, D. L. Feng, E. D. Lu, T. Yoshida, H. Eisaki, A. Fujimori, K. Kishio, J.-I. Shimoyama, T. Noda, S. Uchida, Z. Hussain, and Z.-X. Shen, *Nature (London)* **442**, 510 (2001).
- ⁴⁴ T. Cuk, F. Baumberger, D. H. Lu, N. Ingle, X. J. Zhou, H. Eisaki, N. Kaneko, Z. Hussain, T. P. Devereaux, N. Nagaosa and Z.-X. Shen, *Phys. Rev. Lett.* **93**, 117003 (2004).
- ⁴⁵ J. Lee, K. Fujita, K. McElroy, J. A. Slezak, M. Wang, T. Aiura, H. Bando, M. Ishikado, T. Masui, J.-X. Zhu, A. V. Balatsky, H. Eisaki, S. Uchida and J. C. Davis, *Nature (London)* **442**, 546 (2006).
- ⁴⁶ W. S. Lee, W. Meevasana, S. Johnston, D. H. Lu, I. M. Vishik, R. G. Moore, H. Eisaki, N. Kaneko, T. P. Devereaux and Z.-X. Shen, *Phys. Rev. B* **77**, 140504(R) (2008).
- ⁴⁷ X. J. Zhou, J. Shi, T. Yoshida, T. Cuk, W. L. Yang, V. Brouet, J. Nakamura, N. Mannella, S. Komiyama, Y. Ando, F. Zhou, W. X. Ti, J. W. Xiong, Z. X. Zhao, T. Sasagawa, T. Kakeshita, H. Eisaki, S. Uchida, A. Fujimori, Z. Zhang, E. W. Plummer, R. B. Laughlin, Z. Hussain and Z.-X. Shen, *Phys. Rev. Lett.* **95**, 117001 (2005).
- ⁴⁸ W. Meevasana, N. J. C. Ingle, D. H. Lu, J. R. Shi, F. Baumberger, K. M. Shen, W. S. Lee, T. Cuk, H. Eisaki, T. P. Devereaux, N. Nagaosa, J. Zaanen and Z.-X. Shen, *Phys. Rev. Lett.* **96**, 157003 (2006).
- ⁴⁹ Y. Chen, A. Iyo, W. Yang, A. Ino, M. Arita, S. Johnston, H. Eisaki, H. Namatame, M. Taniguchi, T. P. Devereaux, Z. Hussain, and Z.-X. Shen, *Phys. Rev. Lett.* **103**, 036403 (2009).
- ⁵⁰ W. S. Lee, K. Tanaka, I. M. Vishik, D. H. Lu, R. G. Moore, H. Eisaki, A. Iyo, T. P. Devereaux, and Z. X. Shen, *Phys. Rev. Lett.* **103**, 067003 (2009).
- ⁵¹ K. Byczuk, M. Kollar, K. Held, Y.-F. Yang, I. A. Nekrasov, Th. Pruschke and D. Vollhardt, *Nature Physics* **3**, 168 (2007).
- ⁵² M. Eschrig, *Adv. Physics* **55**, 47 (2006), and references therein.
- ⁵³ S. Engelsberg and J. R. Schrieffer, *Phys. Rev.* **131**, 993 (1963).
- ⁵⁴ A. Kaminski, M. Randeria, J. C. Campuzano, M. R. Norman, H. Fretwell, J. Mesot, T. Sato, T. Takahashi, and K. Kadowaki, *Phys. Rev. Lett.* **86**, 1070 (2001); T. K. Kim, A. A. Kordyuk, S. V. Borisenko, A. Koitzsch, M. Knupfer, H. Berger and J. Fink, *Phys. Rev. Lett.* **91**, 167002 (2003); M. R. Norman, H. Ding, J. C. Campuzano, T. Takeuchi, M. Randeria, T. Yokoya, T. Takahashi, T. Mochiku and K. Kadowaki, *Phys. Rev. Lett.* **79**, 3506 (1997); S. V. Borisenko, A. A. Kordyuk, V. Zabolotnyy, J. Geck, D. Inosov, A. Koitzsch, J. Fink, M. Knupfer, B. Bu chner, V. Hinkov, C. T. Lin, B. Keimer, T. Wolf, S. G. Chiuzbăian, L. Patthey and R. Follath, *Phys. Rev. Lett.* **96**, 117004 (2006).
- ⁵⁵ S. Johnston, W. S. Lee, Y. Chen, E. A. Nowadnick, B. Moritz, Z.-X. Shen and T. P. Devereaux, *Advances in Condensed Matter Physics.* **2010**, 968304 (2010).
- ⁵⁶ W. S. Lee, S. Johnston, T. P. Devereaux and Z.-X. Shen, *Phys. Rev. B* **75**, 195116 (2007).
- ⁵⁷ L. Pintschovius, *Phys. Stat. Sol. (b)* **242**, 30 (2005).
- ⁵⁸ M. C. Krantz, C. Thomsen, Hj. Mattausch and M. Cardona, *Phys. Rev. B* **50**, 1165 (1994); I.-S. Yang, H.-G. Lee, N. H. Hur and J. Yu, *Phys. Rev. B* **52**, 15078 (1995); X. Zhou, M. Cardona, D. Colson and V. Viallet, *Phys. Rev. B* **55**, 12770 (1997); V. G. Hadjiev, X. Zhou, T. Strohm, M. Cardona, Q. M. Lin and C. W. Chu, *Phys. Rev. B* **58**, 1043 (1998); M. Limonov, S. Lee, S. Tajima and A. Yamanaka, *Phys. Rev. B* **66**, 054509 (2002).
- ⁵⁹ D. Munzar and M. Cardona, *Phys. Rev. Lett.* **90**, 077001 (2003).
- ⁶⁰ W. L. McMillan, *Phys. Rev. B* **167**, 331 (1968).
- ⁶¹ T. P. Devereaux, T. Cuk, Z.-X. Shen and N. Nagaosa, *Phys. Rev. Lett.* **93**, 117004 (2004)
- ⁶² T. P. Devereaux, A. Virosztek and A. Zawadowski, *Phys. Rev. B* **51**, 505 (1995); **59**, 14618 (1999); S. Barišić and I. Batistić, *Europhys. Lett.* **8**, 765 (1989).
- ⁶³ J. Li and J. Ladik, *Sol. State Comm.* **95**, 35 (1995).
- ⁶⁴ R. Heid, K.-P. Bohnen, R. Zeyher and D. Manske, *Phys. Rev. Lett.* **100**, 137001 (2008).
- ⁶⁵ K.-P. Bohnen, R. Heid and M. Krauss, *Europhys. Lett.* **64**, 104 (2003).
- ⁶⁶ F. Giustino, M. L. Cohen and S. G. Louie, *Nature* **452**, 975 (2008).
- ⁶⁷ C. N. Veenstra, G. L. Goodvin, M. Berciu, and A. Damascelli, *arXiv:1003.0141v1*.
- ⁶⁸ D. Reznik, G. Sangiovanni, O. Gunnarsson and T. P. Devereaux, *Nature* **455**, E6 (2008).
- ⁶⁹ B. S. Shastry, *Phys. Rev. Lett.* **63**, 1288 (1989).
- ⁷⁰ J. Mustre de Leon, S. D. Conradson, I. Batistic, and A. R. Bishop, *Phys. Rev. Lett.* **65**, 1675 (1990).
- ⁷¹ A. I. Liechtenstein, I. I. Mazin, O. K. Anderson, O. Jepsen, *Phil. Mag. B* **70**, 643 (1994).
- ⁷² J. Zhong and H.-B. Schüttler, *Phys. Rev. Lett.* **69**, 1600 (1992); S. Koval and A. Greco, *Sol. State Commun.* **90**, 17 (1994).
- ⁷³ O. Rösch, O. Gunnarsson, X. J. Zhou, T. Yoshida, T. Sasagawa, A. Fujimori, Z. Hussain, Z.-X. Shen, and S. Uchida, *Phys. Rev. Lett.* **95**, 227002 (2005).
- ⁷⁴ O. K. Andersen, A. I. Liechtenstein, O. Jepsen and F. Paulson, *J. Phys. Chem. Solids* **56**, 153 (1995).
- ⁷⁵ P.-O. Löwdin, *J. Chem. Phys.* **19**, 1396 (1951).
- ⁷⁶ We note that in Ref. 61 all energies were referenced to the chemical potential in the eigenfunctions ϕ . This overestimated the fermionic momentum dependence for coupling

- to the breathing modes, as pointed out in Ref. 31 (2008). This also led to an overestimation of the magnitude of the coupling to the B_{1g} modes when a value of the electric field $E = 1.85$ eV/Å was used. We show in Section V that this field value is likely an underestimation, and thus comparable λ values are obtained here and in Ref. 61.
- ⁷⁷ R. S. Markiewicz, S. Sahrakorpi, M. Lindroos, H. Lin and A. Bansil, Phys. Rev. B **72**, 054519 (2005).
- ⁷⁸ M. R. Norman, M. Randeria, H. Ding and J. C. Campuzano, Phys. Rev. B **52**, 615 (1995).
- ⁷⁹ G. D. Mahan, *Many-Particle Physics*, Second Edition, Plenum Press, New York (1990).
- ⁸⁰ To estimate the magnitude of the apical coupling we have determined, for Bi-2212, the Madelung energy difference $\Delta\Phi = 10.09$ eV, the dielectric constant $\epsilon(\infty) = 3.5$, giving $\epsilon_{apex} = \epsilon_p + \Delta\Phi/\epsilon(\infty) = \Delta + 2.88$ eV. Mean field corrections to the site energies then shift these values. This is derived in section VI.
- ⁸¹ A. W. Sandvik, D. J. Scalapino, and N. E. Bickers, Phys. Rev. B **69**, 094523 (2004).
- ⁸² A. A. Abrikosov and V. M. Genkin, Zh. Eksp. Teor. Fiz. **65**, 842 (1973) [Sov. Phys. JETP, **38**, 417 (1974)].
- ⁸³ C. Falter, M. Klenner and Q. Chen, Phys. Rev. B **48**, 16690 (1993); C. Falter, M. Klenner, G. A. Hoffmann and Q. Chen, Phys. Rev. B **55**, 3308 (1997); T. Bauer and C. Falter, Phys. Rev. B **80**, 094525 (2009) C. Falter, M. Klenner and G. A. Hoffmann, Phys. Rev. B **57**, 14444 (1998).
- ⁸⁴ S. I. Mukhin and A. Mesaros and J. Zaanen and F. V. Kusmartsev, Phys. Rev. B **76**, 174521 (2007).
- ⁸⁵ A. L. Fetter, Ann. Phys. (N.Y.) **88**, 1 (1974).
- ⁸⁶ D. N. Aristov and G. Khaliullin, Phys. Rev. B **74**, 045124 (2006).
- ⁸⁷ M. A. Quijada, D. B. Tanner, R. J. Kelley, M. Onellion, H. Berger and G. Margaritondo, Phys. Rev. B **60**, 14917 (1999).
- ⁸⁸ N. N. Kovaleva, A. V. Boris, T. Holden, C. Ulrich, B. Liang, C. T. Lin, B. Keimer, C. Bernhard, J. L. Tallon, D. Munzar and A. M. Stoneham, Phys. Rev. B **69**, 054511 (2004).
- ⁸⁹ B. Moritz, F. Schmitt, W. Meevasana, S. Johnston, E. M. Motoyama, M. Graven, D. H. Lu, C. Kim, R. T. Scalettar, Z.-X. Shen and T. P. Devereaux, New Journ. Phys. **11**, 093020 (2009).
- ⁹⁰ S. Johnston, F. Vernay and T. P. Devereaux, Europhys. Lett., **86**, 37007 (2009); K. Foyevtsova, R. Valenti and P. J. Hirschfeld **79**, 144424 (2009).
- ⁹¹ J. D. Jorgensen, M. A. Beno, D. G. Hinks, L. Soderholm, K. J. Volin, R. L. Hitterman, J. D. Grace, I. K. Schuller, C. U. Segre, K. Zhang, and M. S. Kleefisch, Phys. Rev. B **36**, 3608 (1987); E. Kaldis, J. Röhler, E. Liarokapis, N. Poulakis, K. Conder and P. W. Loeffen, Phys. Rev. Lett. **79**, 4894 (1997); O. Chmaissem, J. D. Jorgensen, S. Short, A. Knizhnik, Y. Eckstein and H. Shaked, Nature (London) **397**, 45 (1999).
- ⁹² P. Ewald, Ann. Phys. **369**, 253 (1921).
- ⁹³ J. Li and J. Ladik, Sol. State. Comm. **95**, 35 (1995);
- ⁹⁴ O.I. Lyakhovitskaya, Yu.Z. Nozik, Kristallografiya **32**, 498 (1990).
- ⁹⁵ M. Francois, K. Yvon, P. Fischer, and M. Decroux, Solid State Commun. **63**, 35 (1987).
- ⁹⁶ J. D. Jorgensen, H. -B. Schüttler, D. G. Hinks, D. W. Capone II, K. Zhang, M. B. Brodsky, and D. J. Scalapino, Phys. Rev. Lett. **58**, 1024 (1987).
- ⁹⁷ C. C. Torardi, M. A. Subramanian, J. C. Calabrese, J. Gopalakrishnan, E. M. McCarron, K. J. Morrissey, T. R. Askew, R. B. Flippen, U. Chowdhry, and A. W. Sleight, Phys Rev B **38**, 225 (1988).
- ⁹⁸ N. N. Kovaleva, A. V. Boris, T. Holden, C. Ulrich, B. Liang, C. T. Lin, B. Keimer, C. Bernhard, J. L. Tallon, D. Munzar, and A. M. Stoneham, Phys Rev B **69**, 054511 (2004).
- ⁹⁹ T. Watanabe, T. Fujii and A. Matsuda, Jour. Phys. Soc. Jpn. **72**, 2924 (2003).
- ¹⁰⁰ Q. Huang, J. W. Lynn, Q. Xiong and C. W. Chu, Phys. Rev. B **52**, 462 (1995).
- ¹⁰¹ P.G. Radaelle, J.L. Wagner, B.A. Hunter, M.A. Beno, G.S. Knapp, J.D. Jorgensen and D.G. Hinks, Physica C **216**, 29 (1993).
- ¹⁰² A. R. Armstrong, W. I. F. David, I. Gameson, P. P. Edwards, J. J. Capponi, P. Bordet, and M. Marezio, Phys. Rev. B **52**, 15551 (1995).
- ¹⁰³ M. Paranthaman, B.C. Chakoumakos, Journ. Sol. State Chem. **122**, 221 (1996).
- ¹⁰⁴ Q. Huang, O. Chmaissem, J. J. Capponi, C. Chaillout, M. Marezio, J. L. Tholence, and A. Santoro, Physica C **227**, 1 (1994).
- ¹⁰⁵ Y. Shimakawa, Y. Kubo, T. Manako, Y. Nakabayashi, and H. Igarashi, Physica C **156**, 97 (1988).
- ¹⁰⁶ D. E. Cox, C. C. Torardi, M. A. Subramanian, J. Gopalakrishnan, and A. W. Sleight, Phys. Rev. B **38**, 6624 (1988).
- ¹⁰⁷ Y.-Q. Tang, B.-X. Lin, D.-Y. Zhou, W.-J. Zhu, F.-X. Chew, X.-M. Zheng, Y.-F. Zheng, N. Li, K.-X. Chen and G. Lu, Science In China Series A, **22**, 409 (1990).
- ¹⁰⁸ T. P. Devereaux, A. Virosztek, A. Zawadowski, M. Opel, P. F. Müller, C. Hoffmann, R. Philipp, R. Nemetschek, R. Hackl, H. Berger, L. Forró, A. Erb and E. Walker, Solid State Comm. **108**, 407 (1998); M. Opel, R. Hackl, T. P. Devereaux, A. Virosztek, A. Zawadowski, A. Erb, E. Walker, H. Berger and L. Forró, Phys. Rev. B **60**, 9836 (1999).
- ¹⁰⁹ W. A. Harrison, *Elementary Electronics Structure*, World Scientific (2004).
- ¹¹⁰ Y. He, T. S. Nunner, P. J. Hirschfeld and H.-P. Cheng, Phys. Rev. Lett. **96**, 197002 (2006).
- ¹¹¹ T. S. Nunner, J. Schmalian and K. H. Bennemann, Phys. Rev. B **59**, 8859 (1999).
- ¹¹² Yunkyu Bang, Phys. Rev. B **78**, 075116 (2008).
- ¹¹³ S. Johnston and T. P. Devereaux, Phys. Rev. B **81**, 214512 (2010).
- ¹¹⁴ T. Das, R. S. Markiewicz and A. Bansil, Phys. Rev. Lett. **98**, 197004 (2007).
- ¹¹⁵ A. Comanac, L. De' Medici, M. Capone and A. J. Millis, Nature Physics **4**, 287 (2008).
- ¹¹⁶ T. A. Maier, D. Poilblanc and D. J. Scalapino, Phys. Rev. Lett. **100**, 237001 (2008).
- ¹¹⁷ J. P. Carbotte, Rev. Mod. Phys. **62**, 1027 (1990).
- ¹¹⁸ S. V. Vonsovsky, Yu. A. Izyumov and E. Z. Kurmaev, *Superconductivity of Transition Metals, Their Alloys and Compounds*, (Springer-Verlag, Berlin, 1982).
- ¹¹⁹ P. J. Williams and J. P. Carbotte, Phys. Rev. B **43**, 7960 (1991); E. J. Nicol and J. P. Carbotte, Phys. Rev. B **44**, 12511 (1991).
- ¹²⁰ O. V. Dolgov, I. I. Mazin, A. A. Golubov, S. Y. Savrasov and E. G. Maksimov, Phys. Rev. Lett. **95**, 257003 (2005).
- ¹²¹ M. Capone, M. Fabrizio, C. Castellani and E. Tosatti, Science **296**, 2364 (2002).

- ¹²² M. Capone, M. Fabrizio, C. Castellani and E. Tosatti, *Rev. Mod. Phys.* **81**, 943 (2009).
- ¹²³ J.-H. She and J. Zaanen, *Phys. Rev. B* **80**, 184518 (2009).
- ¹²⁴ F. C. Zhang and T. M. Rice, *Phys. Rev. B* **37**, 3759 (1988).
- ¹²⁵ H. Eskes and J. H. Jefferson, *Phys. Rev. B* **48**, 9788 (1993).
- ¹²⁶ P. Piekarczyk, J. Konior and J. H. Jefferson, *Phys. Rev. B* **59**, 14697 (1999).